Causes of oceanic crustal thickness oscillations along a 74-Myr Mid-Atlantic Ridge flow line

William J Shinevar, Hannah F Mark, Fiona Clerc, Emmanuel A Codillo, Jianhua Gong, Jean-Arthur J Olive, Paris T Smalls, Stephanie M Brown, Yang Liao, Véronique Le Roux, et al.

Causes of oceanic crustal thickness oscillations along a 74-Myr Mid-Atlantic Ridge flow line

William J. Shinevar[1], Hannah F. Mark[1], Fiona Clerc[1], Emmanuel A. Codillo[1], Jianhua Gong[1], Jean-Arthur Olive[2], Stephanie M. Brown[3], Paris T. Smalls[1], Yang Liao[4], Véronique Le Roux[4], Mark D. Behn[4, 5]

[1]Massachusetts Institute of Technology/Woods Hole Oceanographic Institution Joint Program in Oceanography/Applied Ocean Science and Engineering, Woods Hole, MA 02543, USA, [2]Laboratoire de Géologie, Ecole normale supérieure/CNRS UMR 8538, PSL Research University, Paris, France, [3]Department of Earth, Atmospheric, and Planetary Sciences, Massachusetts Institute of Technology, 77 Massachusetts Avenue, Cambridge, MA 02139, United States, [4]Department of Geology and Geophysics, Woods Hole Oceanographic Institution, Woods Hole, MA 02543, USA, [5]Department of Earth and Environmental Sciences, Boston College, Chestnut Hill, Massachusetts 02467, USA

Key Points:

1. We conducted one of the longest continuous geophysical surveys along a 74-Myr spreading-parallel flow line across the Mid-Atlantic Ridge.

2. Spectral densities of bathymetry and gravity data show concurrent peaks at 390-, 550-, and 950-kyr periods, and diffuse power at >1 Myr.

3. A negative correlation between fault spacing and gravity-derived crustal thickness suggests a link between magma input and fault style.

Abstract:

Gravity, magnetic, and bathymetry data collected along a continuous 1400-km-long spreading-parallel flow line across the Mid-Atlantic Ridge indicate significant tectonic and magmatic fluctuations in the formation of oceanic crust over a range of timescales. The transect spans from 28 Ma on the African Plate to 74 Ma on the North American plate, crossing the Mid-Atlantic Ridge at 35.8 ºN. Gravity-derived crustal thicknesses vary from 3–9 km with a standard deviation of 1 km. Spectral analysis of bathymetry and residual mantle Bouguer anomaly (RMBA) show diffuse power at >1 Myr and concurrent peaks at 390, 550, and 950 kyr. Large-scale (>10-km) mantle thermal and compositional heterogeneities, variations in upper mantle flow, and detachment faulting likely generate the >1 Myr diffuse power. The 550- and 950-kyr peaks may reflect the presence of magma solitons and/or regularly spaced ~7.7 and 13.3 km short-wavelength mantle compositional heterogeneities. The 390-kyr spectral peak corresponds to the characteristic spacing of faults along the flow line. Fault spacing also varies over longer periods (>10 Myr), which we interpret as reflecting long-lived changes in the

fraction of tectonically- vs. magmatically- accommodated extensional strain. A newly discovered off-axis oceanic core complex (Kafka Dome) found at 8 Ma on the African plate further suggests extended time periods of tectonically dominated plate separation. Fault spacing negatively correlates with gravity-derived crustal thickness, supporting a strong link between magma input and fault style at mid-ocean ridges.

1. Introduction

The oceanic lithosphere covers more than two-thirds of the Earth's surface and plays an essential role in plate tectonics. Oceanic lithosphere forms at mid-ocean ridges (MORs) through a combination of magmatic and tectonic activity (Macdonald et al., 1996; Searle, 2013). Variability in the magma supply associated with differences in spreading rate, axial thermal structure, and/or mantle melting processes has been linked to first-order differences in ridge morphology (e.g., Chen & Morgan, 1990a; Chen & Morgan, 1990b; Ito & Behn, 2008; Roth et al., 2019), fault behavior (e.g., Buck et al., 2005; Behn & Ito, 2008; Tucholke et al., 2008), and the chemistry of mid-ocean ridge basalts (e.g., Bonatti et al., 2003; Behn & Grove, 2015).

Temporal variability in magmatic and tectonic forcing at mid-ocean ridges has been hypothesized and/or observed on timescales from millions to thousands of years. For example, Bonatti et al. (2003) found a long-term increase in gravity-derived crustal thickness along the Vema Transform Fault (Guinea Fracture Zone) in the Atlantic, which they hypothesized to result from a long-term (>20 Myr) increase in mantle potential temperature. Previous studies in the Mid-Atlantic also found 2–4 Myr period variations in gravity-derived crustal thickness, which were interpreted as representing changes in mantle upwelling and flow (Bonatti et al., 2003; Pariso et al., 1995) or as reflecting alternating phases of dominantly magmatic and amagmatic extension (Tucholke et al., 1997). Further, Minshull et al. (2006) attributed seismically derived crustal thickness variations with periods of ~3 Myr near the ultraslow-spreading Southwest Indian Ridge to be the result of episodic melt flow and tectonic extension during amagmatic periods.

On slightly shorter time-scales, Canales et al. (2000a) reported seismically-derived crustal thickness variations with periods of ~0.5–1 Myr near the axis of the Mid-Atlantic Ridge close to the Kane fracture zone, which they attributed to temporal variability in magma supply. Measured cross sections of the Oman ophiolite also depict thickness variations over 5–10 km scale attributed to accretion above mantle diapirs (Nicolas et al., 1996). Assuming a half spreading rate between 25 and 50 mm yr^{-1} for the crust formed in the Oman ophiolite, the 5–10 km scale thickness variations correspond to variations with a periodicity of 100–400 kyr. High-resolution sampling across the intermediate-spreading Juan de Fuca Ridge (Ferguson et al., 2017) revealed a rapid change (<10 kyr) in basalt geochemistry coincident with 1-km increase in crustal thickness (Carbotte et al., 2008), demonstrating that changes in magma supply can also occur on very short time scales.

Some short period (<100 kyr) variations in crustal production have been proposed to result from external forcing on the MOR magmatic system. Crowley et al. (2015) hypothesized that fluctuations in sea level caused by Milanković cycles (23, 41, and 100 kyr) could modulate the amount of magma produced by adiabatic decompression melting below MORs by modulating mantle pressure. Tolstoy (2015) also suggested that orbital forcing affects crustal stresses and thus the dynamics of melt extraction on Milanković time scales, particularly at fast-spreading ridges.

One challenge in deciphering temporal changes in the structure and evolution of oceanic lithosphere is that most previous studies have focused on the formation of young lithosphere at or near the ridge axis. For example, to understand the magmatic input to mid-ocean ridges, studies have focused on variations in the chemistry of mid-ocean ridge basalts (e.g., Langmuir et al., 1992; Gale et al., 2013), near-axis seismic and gravity measurements of crustal thickness (e.g., Kuo & Forsyth, 1988; Detrick et al., 1995; Hooft et al., 2000), and the physical dynamics of magma chambers and their eruptions (e.g., Sinton & Detrick, 1992; Rubin & Pollard, 1988; Tan et al., 2016). Near-axis geophysical observables, such as gravity, bathymetry, and fault style, have also been analyzed to understand the way magmatism and tectonics interact to shape the ridge axis (e.g., Kuo & Forsyth, 1988; Detrick et al., 1995; Hooft et al, 2000; Buck et al., 2005; Howell et al. 2016; 2019). By contrast, relatively few studies have investigated off-axis oceanic lithosphere (e.g., Morris et al., 1993; Tucholke et al., 1997; Lizzaralde et al., 2004) where mass wasting and sedimentation restrict sampling and complicate the bathymetric record of faulting. Thus, temporal variability has typically been inferred from very short across-axis studies (e.g., Canales et al., 2000a; Crowley et al., 2015), as well as comparison of spatial variations between different ridge segments of similar spreading rates (e.g. Purdy et al., 1992).

To better quantify the temporal variability in magma supply and fault style in oceanic lithosphere over timescales of 10^4–10^7 years, we acquired a 1400-km-long geophysical transect collecting bathymetry, gravity, and magnetic data during the SCARF cruise (Student-led Cruise Along a Ridge Flow Line) (#AR023-02) aboard the R/V *Neil Armstrong* in October 2017. The cruise track followed a single, spreading-parallel flow line between 30˚ and 45˚W crossing the Mid-Atlantic Ridge (MAR) at 35.8˚N, ~100 km north of the Oceanographer Fracture Zone (Figure 1). The cruise yielded one of the longest geophysical surveys along a single ridge flow line and covered ~28 Ma lithosphere on the African plate to 74 Ma lithosphere on the North American plate. Our analysis of this flow line allows us to estimate key properties of the oceanic lithosphere, including crustal thickness, effective elastic plate thickness, and fault characteristics to provide constraints on the tectonic and magmatic processes that control temporal variation of crustal formation at the same mid-ocean ridge segment.

2. Geologic Setting

The Central Atlantic Ocean, the portion of the Atlantic Ocean south of the Azores plateau and north of Guinean Fracture Zone, began spreading at ~190 Ma (Labails et al., 2010), likely triggered by the 203 and 193 Ma surges of Central Atlantic magmatic province volcanism (Jourdan et al., 2009). Early accretion in the Central Atlantic Ocean was highly asymmetric, adding significantly more material to the North American plate. The Central Atlantic Ocean originally accreted slowly (half spreading rate of 4 mm yr^{-1}) until 170 Ma, when the spreading direction shifted from northwest-southeast to east-west and spreading rate doubled. Afterwards, the half spreading rate remained around 10 mm yr^{-1} with periods of faster rates up to 30 mm yr^{-1} (Labails et al., 2010; Seton et al., 2012).

The Mid-Atlantic Ridge north of the Oceanographer Fracture Zone and south of the Tydeman Fracture Zone consists of 20–45 km long segments separated by non-transform offsets. The SCARF cruise track followed a flow line that crossed the ridge axis near the center of the third segment north of the Oceanographer Fracture Zone at 35.8˚N, 34.2˚W. The crossing point lies approximately 90 km north of the Oceanographer Fracture Zone and 260 km south of Tydeman Fracture Zone. This segment has been named previously as the South Alvin Mid-Atlantic Ridge (S. AMAR) (e.g., Detrick et al., 1995) and AMARR91 by Gale et al. (2013). The S. AMAR segment is 40-km long and has a continuous, hourglass-shaped axial rift valley (Paulatto et al., 2015; Eason et al., 2016).

The surrounding near-axis region of the Mid-Atlantic Ridge has been well studied. The Rainbow Hydrothermal Vent Field (German et al., 1996) is situated approximately 50 km northeast of the S. AMAR segment, and the French-American Mid-Ocean Undersea Study (Project FAMOUS) (Ballard et al., 1975) investigation area was located two segments further to the north. The axial rift valley is shallow where it intersects the SCARF cruise track, approximately 2580 m deep and 8 km wide. The segment currently has a slightly asymmetric ridge-perpendicular half spreading rate of 14 mm yr^{-1} eastward and 13 mm yr^{-1} westward as calculated from magnetic isochrones in this study (see Section 3.1). Rare-earth element and isotopic chemistry of dredged MORB samples for this segment, as well as other nearby segments show heterogeneity, suggesting at least three mantle components, one of which comes from the Azores plume (White & Schilling, 1978; Bougault et al, 1988; Shirey et al., 1987).

3. Observations: Underway Geophysical Data Collection

3.1 Magnetics

We used sea surface total magnetic field data to constrain seafloor age along the SCARF cruise track. The data were acquired using a SeaSPY Overhauser magnetometer towed at an offset of 300 meters behind the ship. The raw sea surface total magnetic field data was corrected for (1) navigation offset from ship-to-magnetometer layback, (2) outlying data points, (3) the international geomagnetic reference field (IGRF-11 model, Finlay et al., 2010), and (4) diurnal field variations (relative to Fredericksburg, Virginia, USA, (FRD)). Sea surface crustal magnetic anomalies were obtained by correcting the total field data for the paleo-inclinations (30.5°–35.2°) and -declinations (49.7°–54.63°) estimated for the Atlantic using the method of Schettino (2014) and the paleopoles of Schettino and Scotese (2005). The resulting magnetic anomalies along the SCARF transect are in good agreement with the EMAG2v3 (version 3) global magnetic anomaly grid (Meyer et al., 2016) when smoothed (Figure A1) and with magnetic anomaly measurements from nearby or crossing ship paths from NCEI's Marine Trackline Geophysical database (https://www.ngdc.noaa.gov/mgg/geodas/trackline.html) (Figure 1b).

We estimated the ages represented by the magnetic anomalies along the SCARF transect by matching the observed anomalies to a calculated synthetic magnetic anomaly profile. The synthetic model assumes a magnetization square wave based on a magnetized layer at a constant depth of 3.5 km. The layer is 1 km thick and has a magnetization of ±5 A/m with polarities based on the Müller et al. (2008) ocean age database and the Wei (1995) Geomagnetic Polarity Time Scale. We filtered this synthetic magnetization profile with a 2-km Gaussian window to account for emplacement effects, following the approach of Tivey & Tucholke (1998). The synthetic magnetization was converted to a synthetic magnetic anomaly profile using the Parker (1972) Fourier summation approach.

To assign isochron numbers and ages to magnetic anomalies along the SCARF cruise track, we visually correlated the synthetic magnetic anomaly profile with the measured magnetic anomalies (Figure 2). We defined the ridge axis as the midpoint of the axial valley and set its age to 0 Ma. Spreading rates were predicted on the basis of the correlated magnetic anomalies and agree well with those calculated along the SCARF transect using the global seafloor age model of Müller et al. (2008) (Figure 3d).

3.2 Bathymetry and Fault Identification

Bathymetry data (Figure 3a) were collected using a Kongsberg EM122 12-kHz multibeam echosounder. This multibeam echosounder has 0.2% error directly below the ship with a maximal 0.6% error at 60–70˚. Center beam bathymetry was collected at 1 Hz and multi-beam bathymetry was collected at 0.33 Hz. The data were cleaned for outlying data points and gridded with the MB-System software (Caress and Chayes, 2017). Figure A2.1-18 shows images of all the trackline multi-beam bathymetry (bathymetry data available through Marine Geoscience Data System). The swath width is ~6 times the water depth. We identified individual faults manually using a combination of the center beam and multibeam bathymetry. We identified axis-facing fault scarps as changes in topographic gradient observed in the center beam bathymetry data that correspond to linear features in the multibeam bathymetry. Abyssal hills may not be entirely fault-controlled, and some may be relict volcanic ridges. Volcanic ridges should manifest as symmetric ridges, displaying both inward- and outward-facing slopes within a few km of one another. Although common at fast spreading rates, volcanic ridges are typically not preserved at slower spreading rates (Carbotte & Macdonald, 1994), and such morphological features were not seen along the transect. Here we interpret all fault scarp picks as abyssal hill-bounding faults. We estimate the throw (vertical offset) and heave (horizontal offset) of each fault by picking the shallowest depth of the fault in the center beam bathymetry as the scarp top and the deepest depth of the fault as the scarp bottom. We only picked faults that have an identifiable throw of greater than 10 m. Using this approach, we identified 415 fault scarps along the SCARF transect (red dots in Figure 3a). Individual fault statistics are available in Supplementary Table 1. We find most fault slopes have less than 30˚ angles, likely due to gravitational mass wasting of the fault scarps (Cannat et al., 2013) (Figure A3). We calculated fault spacing (bin length divided by the number of picked faults in a bin, Figure 3b) and total fault heave in overlapping 100 km bins every 25 km along the flow line. There are 12 or more faults in each bin. The resulting bin spacing precludes analysis of short-period (< 2 Myr) variations in fault spacing.

We validated our fault picks by examining the frequency distribution of fault throws (Figure 4). Natural fault populations are predicted to display an exponential frequency distribution for faults having lengths comparable to or greater than the brittle layer thickness (Cowie et al., 1993; Carbotte & Macdonald, 1994) and exponential distributions in scarp heights and fault spacing have been observed at the East Pacific Rise and Chile Ridge (Bohnenstiehl & Kleinrock, 1999; Bohnsenstiehl & Carbotte, 2001; Howell et al., 2016). Consistent with these results, we observe that scarp frequency decays exponentially with scarp throw for our picks, suggesting that our scarp database is sampling the true fault population. The exponential decay of fault population fades at large throw (>0.7 km); we only find three faults with throw greater than 0.7 km.

A major difference between previous fault population studies and ours is that most previous studies analyzed only near axis faults along multiple ridge segments, while most of our picked faults are located far from the ridge axis in >10 Ma lithosphere. For instance, the furthest off axis fault analyzed by Howell et al. (2016) is 100 km away from the ridge axis, corresponding to ~3 Ma lithosphere. To check the validity of our off-axis fault picks, we compared the distributions of fault throw for (1) all faults within 200 km of the ridge, (2) all faults within 400 km of the ridge, and (3) the entire transect. We find no change of slope in the cumulative throw distributions between those calculated for 200 and 400 km cut-offs below a throw of ~0.6 km. The change in slope for throw > 0.6 km is likely due to the low number of high throw faults found within 400 km of the ridge axis along our transect, making it difficult for a meaningful comparison. Beyond 400 km off-axis, we identify no faults with throw > 0.5 km. In terms of total fault occurrence, we find 138 faults (33% of the total faults found along the transect) at distances >400 km off-axis (45% of our track line). The lack of identified faults off-axis is likely due to sedimentation and mass wasting reworking seafloor topography. This interpretation is supported by the observation that at higher sediment thicknesses (>400 m) there is an apparent increase in fault spacing, while for lower sediment thicknesses (< ~300 m) nearer to the ridge axis (<400 km away), fault spacing does not correlate with sediment thickness (Figure 3b). Thus, we limit our analyses of fault statistics on this transect to within 400 km of the ridge and interpret fault spacing variations within this distance to reflect changes in tectonic behavior.

We calculated the fraction of spreading accommodated by magmatic accretion, *M* (0 for purely tectonic spreading and 1 for purely magmatic spreading; Buck et al., 2005) in each 100-km bin by subtracting the cumulative heave from the bin length and dividing by the bin length. *M* values calculated in this manner are maxima, as apparent fault heave recorded by scarp morphology is reduced through sedimentation and mass wasting. In general, these effects should become more significant in older lithosphere farther off-axis. Focusing on bins within 400 km of the ridge axis, where we have the best estimates of fault statistics, we find that *M* varies from 0.6–0.85 and is smallest near the ridge (Figure 3c). Farther off-axis, variations in fault spacing are likely to be better proxies for variations in tectonic behavior, as spacing will only be affected by mass wasting and sedimentation if an existing fault is degraded or buried such that it can no longer be identified in the center beam data.

3.3 Gravity

Shipboard gravity data was collected at a 1 Hz sampling rate along the SCARF transect using a Bell BGM-3 gravimeter. Corrections were applied for (1) instrument calibration, (2) instrument drift, (3) latitude variations, and (4) the Eötvös effect. We filtered the corrected gravity data with a 2-pole low-pass Butterworth filter with corner frequency 0.004 per sample and removed outlying data points. The free-air anomaly (FAA) was calculated by subtracting the reference gravity along the GRS80 ellipsoid (Moritz, 1980) from the observed gravity. Our data is in excellent agreement with the 1-arcminute satellite–derived marine FAA version 24 (Sandwell et al., 2014) (Figure 1c). The mantle Bouguer anomaly (MBA) was calculated by subtracting the water-sediment, sediment-crust, and crust-mantle density interfaces from the FAA following the spectral method of Parker (1972). We assume a 6-km thick crustal layer. Sediment thickness (Figure 3b) was taken from Divins (2003), which interpolated sediment thickness from compiled isopach maps, ocean drilling records, and seismic reflection data. To reduce edge effects in the calculation of the MBA, we added 500 km of satellite–derived data (Sandwell et al., 2014) to each end of the SCARF transect. Densities used to calculate density contrasts for water, sediment, crust, and mantle were assumed to be 1000, 2100, 2800, and 3300 kg m^{-3}, respectively, with the sediment density taken from Hamilton (1978). To obtain the residual mantle Bouguer anomaly (RMBA) (Figure 3e), we further corrected the MBA for thermal contraction of the oceanic lithosphere assuming a half-space cooling model (Turcotte & Schubert, 2014) with the magnetically derived ages (Figure 2), T_{mantle}= 1350 ˚C, $T_{surface}$ = 0 ˚C, thermal expansivity α = 5x10^{-5} ˚C^{-1}, and thermal diffusivity κ = 10^{-6} m^{2} s^{-1}.

3.4 Gravity-Derived Crustal Thickness

The RMBA can be used to estimate relative variations in crustal thickness assuming a constant crustal density. Relative variations in crustal thickness derived from this approach have been shown to compare well to constraints from co-located seismic studies (e.g., Tolstoy et al., 1993; Hooft et al., 2000; Wang et al., 2011). Here we calculated relative crustal thickness variations by downward continuing the de-meaned RMBA to a constant depth of 10 km below the sea surface (Kuo and Forsyth, 1988; Wang et al., 2011). To remove short-wavelength noise, we filtered the RMBA before downward continuation, using a cosine taper designed such that signals with wavelengths less than 25 km were filtered out and signals with wavelengths greater than 45 km were fully retained. Because the average half spreading rate along the SCARF transect is ~14 km Myr^{-1}, this removes crustal thickness variations occurring at wavelengths less than ~2 Myr. We then calculated crustal thickness variations with respect to a 6 km crust (Figure

3f), corresponding to the average crustal thickness obtained at a nearby ridge segment using seismic refraction data (Hooft et al., 2000). Our results agree well with the regional estimates of gravity-derived crustal thickness calculated by Wang et al. (2011).

3.5 Kafka Dome

Along our transect, we observed a dome-shaped bathymetric high at 35˚ 34' N, 32˚ 54' W (Figure 5), which we name Kafka Dome. Kafka Dome was identified as an oceanic core complex based on its dome morphology with a topographic prominence of ~1 km and a ~7 km length widening away from the axis into an elongated ridge. This morphology is consistent with the breakaway ridge geometry observed at well-developed oceanic core complexes at 13˚20'N and 13˚30'N on the MAR (Figure 5c, Escartín et al., 2017) and Mt. Dent on the Mid-Cayman spreading center (Hayman et al., 2011). The measured size and topographic height of the dome are likely minimal estimates of the original dome structure due to off-axis sedimentation and mass wasting. We also observe a local ~8 mGal increase in the RMBA skewed towards the ridge axis (Figure 5b). Similar RMBA increases at other oceanic core complexes are commonly interpreted as positive mass anomalies caused by thinner crust in the fault footwall (Tucholke et al., 1998; 2008). We do not observe corrugations as seen at many near ridge core complexes (e.g., Cann et al., 1997), likely due to off-axis sedimentation. Taken together, these observations point toward Kafka Dome as a rare example of an inactive off-axis oceanic core complex.

The discovery of a fossil core complex indicates that within the last 10 Ma, faulting style at the S. AMAR segment has changed from an oceanic core complex regime to a regularly spaced abyssal hill regime characteristic of presently accreting seafloor in the vicinity of the Oceanographer Fracture Zone (Escartín et al., 2008). The Rainbow Massif and Pot of Gold Massif are the closest known large-offset detachment faults (Paulatto et al., 2015; Eason et al., 2016). The coincidence of Kafka Dome with the region of larger fault spacing located at 8–22 Myr on both sides of the ridge axis (shaded bars in Figure 3) suggests that this interval may be characteristic of a long-lived oceanic core complex regime.

4. Time-Series Analysis

Using the magnetically derived ages and our shipboard geophysical datasets, we apply spectral analysis to decompose the bathymetry and gravity data in space and time and determine what frequency range(s) hold the most power in our data. Because various tectonic and magmatic processes act on different timescales, the spectral power density can distinguish the relative importance of these processes. We also calculate the coherence and admittance between the gravity and simultaneously-observed center beam bathymetry data, which we use to estimate the elastic plate thickness, T_e, along the flow line.

4.1 Spectral Analysis

Time-domain spectral analysis on the bathymetry and RMBA (Figure 6) was performed using the multitaper method (Percival & Walden, 1993) with seven tapers.

We used ages defined by linear interpolation of our magnetic isochron picks. We investigate spectral power in the time domain such that spreading rate changes do not produce spurious spectral peaks. We first de-trended the bathymetry and gravity data in the time domain. To help identify spectral peaks for bathymetry, the spectra were calculated on the time-derivative of the bathymetry, which amounts to pre-whitening the data (Percival & Walden, 1993). We limited all spectral analysis to wavelengths that occur five or more times in the analyzed section of the geophysical transect (e.g., <5.6 Myr for the two 0–28 Myr regions adjacent to the ridge axis) and were not filtered out via preprocessing (<300 kyr for gravity and <10 kyr for bathymetry). We define a spectral peak as a region that has a higher value than the 95th percentile confidence interval of the background spectra.

We separated the transect into three sections for analysis: the entire eastern flank (0–28 Ma), the corresponding near ridge western flank (0–28 Ma), and the older, off-axis lithosphere (28–51 Ma) on the western flank. The window of the east flank (blue portion of Figure 6) is set by the length of our transect. The window of the near-axis west flank (red portion of Figure 6) is set equal to the eastern flank for comparison purposes. Further west, the cruise encountered stormy weather that added high frequency noise to our gravity data that the Butterworth filter was unable to remove, so we omit these from the subsequent analysis. Setting these boundaries allows us to employ a standard multi-taper method and intuitively present the analysis and confidence intervals. We find that the two near-axis sections (red and blue, Figure 6) display similar bathymetry and RMBA power spectra. The off-axis section (orange, Figure 6) lacks the same peaks in the bathymetry and has weaker power overall, likely due to mass wasting and sedimentation.

For the North American (western) 0–28 Ma bathymetry power spectra, broad peaks appear at 300-, 390-, 550-, and 950-kyr periods (dashed vertical black lines in Figure 6b). For the African (eastern) bathymetry power spectra, broad peaks appear at 270-, 340-, 550-, and 950-kyr periods. The near-axis RMBA power spectra show peaks at 390-, 550-, and 950-kyr periods on both the North American and African plates. Power is diffuse as spectral densities lack peaks but remain high at longer periods (> 1 Myr) for both the bathymetry and RMBA. The off-axis North American 28–51 Ma RMBA spectral density (orange in Figure 6d) shows a strong peak at 390 kyr and a diffuse peak at 650 kyr (dash-dotted line in Figure 6d).

The shortest period peaks in both the RMBA and bathymetry likely reflect abyssal hill spacing. The typical spacing of abyssal hill-bounding faults along the transect is 2–6 km (Figure 3b). For a half spreading rate of ~14 mm yr^{-1}, this implies that faulting should add power to the bathymetry spectra between 140–420 kyr. This is consistent with the spectral power in the bathymetry between 250–400 kyr, as well as the 390-kyr spectral peaks in the RMBA, suggesting that faulting modifies the crustal thickness at these periods.

The 550- and 950-kyr peaks in the RMBA of the near-axis sections and the 650-kyr diffuse peak in the off-axis section do not correlate with the abyssal hill fabric and may instead reflect processes that result in variations in crustal thickness (see discussion in Section 5). The change in RMBA spectral peaks between the younger, near-axis (0–28 Ma) and the older, off-axis (28–51 Ma) suggests a change in the tectono-magmatic processes causing these peaks. There may also be power at longer wavelengths (e.g., 10–20 Myr) as seen by the periodicity in the raw RMBA data (Figure 3e); however, the section length limits us to interpreting periods in the power spectra less than 5.6 Myr.

There are no significant peaks in the bathymetry power spectrum at any of the Milanković cycle periods (100 kyr, 41 kyr, and 23 kyr) as reported by Crowley et al. (2015), supporting the idea that ocean floor bathymetry formed at slow-spreading MORs is not sensitive to fluctuations in melt supply triggered by sea level change (Olive et al., 2015; 2016; Goff, 2015; Goff et al., 2018).

4.2 Admittance & Coherence

Elastic plate thickness, T_e, provides an estimate for the thickness of a rigid elastic plate (overlying an inviscid half-space) that best fits the observed patterns of lithospheric flexure. It is therefore a useful proxy for the integrated strength of the plate, and a direct control on the morphology of the seafloor (Watts, 2001). To estimate T_e, we calculated the admittance and coherence of the topography and MBA along the entire SCARF transect following the approach of Forsyth (1985) (Figure 7). Admittance is defined as the transfer function between topography and MBA. The highest value of admittance is reached through isostatic compensation, which produces topography in response to local thickening of the crust. Short-wavelength oscillations in crustal thickness, however, tend to be flexurally compensated, suppressing strong topographic signals. Thus, admittance is usually low in the short-wavelength limit. Thinner elastic plates will have a larger amplitude admittance at shorter wavelengths because they can isostatically compensate shorter wavelength topography.

Coherence is a statistic that characterizes the strength of the association between two spectra at different wavelengths. For an elastic plate, long wavelength topographic variations will be isostatically compensated, and thus bathymetry and the MBA will have a coherence of 1. On the other hand, short wavelength topography that is not isostatically compensated will have a coherence of 0. For the calculation of admittance and coherence, the bathymetry and MBA data were not pre-whitened and the densities of the crust and mantle were assumed to be 2800 and 3300 kg m^{-3}, respectively. For comparison, we also calculated theoretical coherence and admittance curves for an idealized elastic plate model of a given T_e, assuming a Young's modulus of 100 GPa, Poisson's ratio of 0.25, a crustal thickness of 6 km, and equal loading on the surface and base of the plate. Estimates of T_e from coherence are relatively insensitive to changing the assumed ratio of loading on the surface and base of the plate and to reasonable oceanic crustal thickness variations (4–8 km) (Forsyth, 1985). Coherence and admittance estimates of T_e are also insensitive to the inclusion or exclusion of the off-axis (28–74 Ma) data.

An elastic plate thickness (T_e) of 6–12 km best fits both the admittance and coherence (Figure 7). T_e calculated from the admittance and coherence analyses reflects the strength of the plate at the time of loading. Our results are in the range found for T_e in the Atlantic based on applying elastic flexure theory to off–axis volcanoes emplaced on young (<10 Ma) oceanic crust (Calmant & Cazenave, 1987). Smith et al. (2008)

found evidence of highly-rotated low offset faults in the Central Atlantic which would suggest T_e < 1 km at ages <1 Myr . Thus, because our admittance and coherence analyses for the entire SCARF transect predicts a T_e in agreement with young lithosphere, we interpret that the loading was applied near, but not on the ridge axes, most likely during tectono-magmatic processes associated with the creation of the oceanic lithosphere.

5. Discussion

5.1 Variations in Crustal Thickness

Gravity-derived crustal thickness varies between 3 and 9 km with a standard deviation of 1.0 km assuming a mean of 6 km along the SCARF transect (Figure 3f). These fluctuations are consistent with the range of crustal thicknesses observed in seismic studies in Atlantic crust away from hotspots (e.g., Hooft et al., 2000; Canales et al., 2000a,b; Lizzaralde et al., 2004), as well as previous gravity-derived crustal thickness analyses for the Atlantic Ocean (Lin et al., 1990; Detrick et al., 1995; Wang et al., 2011). We observe spectral peaks in the near-axis RMBA data at 390-, 550-, and 950-kyr periods and diffuse power at periods longer than 1 Myr. These observations are consistent with seismic imaging of oceanic crust, which find crustal thickness variations on timescales of 0.5–1 Myr in the Atlantic (e.g., near the Kane fracture zone: Canales et al., 2000a).

Variations in RMBA-derived crustal thickness could be caused by any one of the following tectonic and magmatic processes: variations at slow to ultra-slow spreading rates, along-segment thickness variations, faults offsetting the Moho, changes in ridge geometry and upper mantle flow, magma solitons, or thermal and chemical variations in the mantle source region (Figure 8). Below we discuss these different processes and their potential influence on the observed crustal thickness variations along the SCARF transect.

Spreading rate is not a dominant cause of crustal thickness variation. Our data show no significant correlation between spreading rate and crustal thickness (Figure A4). This agrees with observations and geodynamic melting models that show crustal thickness is not sensitive to spreading rate for spreading rates greater than 10 mm yr^{-1} (Parmentier & Morgan, 1990; Chen, 1992; Behn & Grove, 2015).

Second, the inferred crustal thickness variations could be due to our transect wandering slightly off the flow line, either closer to the middle or edge of the ridge segment. Indeed, crustal thickness variations between 3 and 9 km have been observed on single ridge segments in the North Atlantic (Cannat, 1996; Hooft et al., 2000). Thus, if the transect was not always perfectly aligned with the segment center, this could explain some of the variability in our observations. This variation should not have a clear expression in the frequency domain due to its stochastic nature, and thus we do not consider it to be the primary source of crustal thickness variations along the SCARF transect.

Variations in ridge segment geometry and upper mantle flow have also been theorized to affect crustal thickness on both segment and regional scale (e.g., Detrick et al., 1995; Hooft et al., 2000; Bonatti et al., 2003). Rearrangement and/or changes in the length of segments could therefore bias our one-dimensional transect of crustal thickness observations. The timescales for such changes is typically on the order of millions of years (Schouten & Klitgord, 1982; Caress et al., 1988; Tucholke et al., 1997). Segment reorientation is observed through changes in the ridge-parallel magnetic lineation. For example, a lineation-perpendicular offset formed by the growth of a fracture zone or the rotation of the ridge-parallel magnetic lineations due to ridge rotation or rift propagation (e.g. Kleinrock et al., 1997). Global magnetic data (Meyer et al., 2016) along our trackline show no alteration in ridge-parallel magnetic lineations. Thus, there is no evidence of ridge segment length variability on either side of the ridge axis based on global magnetic data. Furthermore, ridge segment rearrangement is not periodic, so if it did occur, it would not be expected to manifest as discrete spatial peaks.

Normal faulting can locally alter crustal thickness by offsetting the base of the crust. Previous seismic oceanic crustal thickness studies have shown faulting to be a major driver of observed cross-axis crustal thickness variations because crustal thickness anomalies are often found with fault scarps directly above them (e.g., Canales et al., 2000a, Seher et al., 2010). As shown in Figure 3b, fault spacing within 400 km of the ridge axis ranges from 2–6 km along the SCARF transect. For an average half spreading rate of ~14 km Myr^{-1}, the spectral power associated with such faulting should lie in periods of 140–420 kyr, coincident with spectral peaks in the bathymetry data between 250–400 kyr and the RMBA spectrogram peak at 390 kyr. However, the observed faulting periods do not coincide with the additional spectral peaks at 550 and 950 kyr. In the most extreme case, large-offset (>5 km) detachment faults can cause observable crustal thickness variations up to 1–3 km lasting for 1–3 Myr (Tucholke et al., 1998; Parnell-Turner et al., 2018). Detachment faults create strong asymmetry in crustal thickness, exposing deep crustal units in the footwall of the fault, while the hanging wall can experience emplacement of a complete crustal section (Olive et al., 2010). Because we interpret Kafka Dome as an oceanic core complex in 8 Ma crust east of the ridge axis (see Section 3.6), detachment faulting is a potential factor driving crustal thickness variations. However, the impact of a detachment fault on crustal thickness should be local. In our dataset, this would most likely add diffuse power at periods similar to their lifespan (1–3 Myr) instead of generating clear spectral peaks.

Magma solitons are buoyantly ascending porosity waves of high melt fraction that occur in porous two-phase flow such as the mantle-melting column beneath a mid-ocean ridge (Scott & Stevenson, 1984). These solitons could result in periodic crustal thickness variations if they carry sufficient melt to the ridge axis. Compaction and ascent timescales for basaltic melt in the sub-ridge mantle depend on the melting column height, the melt density contrast, the melt viscosity, the melt fraction, the grain size, and the permeability-porosity relationship (McKenzie, 1985). Depending on the choice of parameters, this timescale can range from 10^4–10^7 years. These timescales reflect the time necessary to extract melt via compaction once, and provide no requirement that the melt extraction process is periodic. More recent two-phase flow models (Sim et al., 2018) at intermediate spreading rates (3.5 cm yr^{-1} half spreading rate) produce stable and persistent porosity waves that produce changes in crustal thickness with an amplitude of ~0.5 km and recurrence time scales on the order of 100s of kyrs. Further two-phase flow modelling is necessary in order to ascertain whether this periodicity exists at slower spreading rates and over which range of parameter values.

Source region heterogeneities, chemical and thermal, have also been invoked to explain observed variations in oceanic crustal thickness. Mantle compositional heterogeneity can cause variations in crustal production by enriching or depleting the mantle source, which modulates the melting fraction below the ridge (Katz & Weartherley, 2012). Thermal heterogeneities associated with mantle hotspots change the melt flux of the upwelling mantle. Bonatti et al. (2003) interpreted a combination of gravity and geochemical data collected along the Vema fracture zone as indicating an increase in mantle potential temperature in this region of the Central Atlantic Ocean over the last 20 Myr, causing an increase in crustal thickness on the timescale of the temperature variations (>10 Myr). However, regional gravity-derived crustal thickness calculations (Wang et al., 2011) suggest more complicated trends in this region.

Plume thermal pulsing has been interpreted to create regional crustal thickness variations that are reflected in the V-shaped ridges near the Azores. However, these V-shaped ridges do not extend south to the S. AMAR segment and Escartín et al. (2001) argue that the melt flux anomaly from the Azores plume stops at approximately 36˚ N, ~30 km north of the SCARF transect. Thus, while thermal pulsing can affect crustal thickness, there is no strong evidence for thermal source heterogeneities along the SCARF transect.

Trace element and isotopic data in dredged gabbros suggest chemical heterogeneities near the SCARF transect caused by influence from the Azores plume or patches of former sub-continental mantle lithosphere (Bougault et al, 1988; Shirey et al., 1987). To cause temporal variations of crustal thickness, these source heterogeneities would have to pass through the melting column entirely; thus the timescales of variation would depend on their size and spacing given a constant mantle upwelling velocity. For instance, in order for the 550- and 950-kyr spectral peaks to correspond to melting anomalies associated with mantle source heterogeneities upwelling at a rate of ~14 km Myr^{-1}, these heterogeneities would need to have a characteristic size and/or spacing of 7.7 and 13.3 km. Larger heterogeneities would cause longer period crustal thickness variations. Because we do not have a long time-series chemical dataset near this ridge-segment, we lack the ability to determine how much of the crustal thickness variations are due to chemical source heterogeneities.

In summary, diffuse power at longer periods (>1 Myr) along the SCARF transect is most likely due to a combination of detachment faulting, mantle source heterogeneities (thermal and/or compositional), and/or magma solitons. The lack of peaks at long periods is likely due to the lack of periodicity and the temporal independence of these processes, allowing the expression of their signals in crustal thickness to constructively or destructively interfere. Faulting is most likely the cause for spectral power in bathymetry and RMBA between 250–400 kyr because this time scale matches the characteristic spacing of fault-bounded abyssal hills. By contrast, only regularly spaced chemical source heterogeneities and/or magma solitons can explain the spectral peaks at 550 and 950 kyr. Further numerical studies are necessary to help estimate the relative importance and plausibility of the different factors contributing to the 550- and 950-kyr periods. The change in RMBA spectral peaks from 550 and 950 kyr in the younger, near-axis sections (0–28 Ma) to a diffuse 650-kyr peak in the older, off-axis section (28–51 Ma) could be caused by a change in these tectono-magmatic processes.

5.2 Variations of Faulting Style and Relation to Magma Supply Variations

Geophysical modeling shows that the main control on fault spacing is the fraction of spreading accommodated by magmatic accretion, *M* (Buck et al., 2005; Behn & Ito, 2008; Ito & Behn, 2008; Tucholke et al., 2008; Olive et al., 2015; Liu & Buck, 2018; Howell et al., 2019). Co-located analyses of ocean floor bathymetry and basalt geochemistry have validated the importance of magma supply on abyssal hill morphology (Roth et al., 2019). With higher *M*, faults are advected off axis into thicker lithosphere more rapidly. This makes continued slip on the existing fault energetically less favorable (Forsyth, 1992; Buck, 1993), resulting in the formation of a new fault near the ridge axis, and an overall decrease in fault spacing and fault offset (Behn & Ito, 2008). A special case occurs when *M* approaches 0.5, such that spreading on one side of the ridge is accommodated purely by magma intrusion, while extension on the conjugate side is entirely accommodated by slip on a long-lived detachment fault whose footwall forms an oceanic core complex (Buck et al., 2005). These models predict an inverse relationship between fault spacing and crustal thickness.

These model predictions imply that if Kafka Dome is indeed the footwall of a detachment fault, the minimum *M* observed should be close to 0.5 (e.g., MacLeod et al., 2009; Schouten et al., 2010). The maximum *M* calculated through fault heave analysis is 0.85 (Figure 3c). This range is in agreement with the overall range in *M* values (0.45–0.75) that has been calculated in young lithosphere along the MAR (Behn & Ito, 2008, Paulatto et al., 2015).

The geophysical data collected along the SCARF transect allows us to further quantify the relationship between magma supply and fault spacing. The Spearman rank correlation coefficient (Spearman, 1904), *r*, detects any type of monotonic correlation rather than only a specific functional correlation and is less sensitive to outliers. Values of r range from -1 to 1, with larger absolute values indicating that the two variables more strongly co-vary according to a monotonically increasing (positive) or decreasing (negative) relationship. The corresponding p-value indicates the probability that the relationship is due to randomness. We find a strong and significant negative correlation (r =-0.64, p=2.2e-4) between average crustal thickness and fault spacing within 400 km of the ridge (Figure 9a). This agrees with previous findings in the Atlantic Ocean of fault spacing increasing at the edge of ridge segments where the crust is thinner (Shaw, 1992; Shaw & Lin, 1993). Thus, we interpret the variations in fault spacing along the flow line (Figure 3b) to reflect variability in magmatic input into the brittle crust of the MAR over time. We find no significant correlation between the calculated M value and crustal thickness over the same bins (r=-0.254, p=0.19) (Figure 9b). This lack of a significant correlation could be due to the coarse resolution of our calculated M values, inaccuracies in our heave measurements due to off-axis sedimentation and mass wasting, or that M is independent of crustal thickness as observed by Howell et al. (2016). Olive et al. (2010) modeled extensional faulting at mid-ocean ridges with separated melt accretion rates in the ductile and brittle layers of oceanic crust and showed that faulting is only sensitive to the M value in the brittle lithosphere. Thus, varying amounts of magma intrusion in the asthenosphere does not affect faulting style and could result in a decoupling of fault style and crustal thickness variations.

Finally, we note that r statistics can be sensitive to outliers. For example, removing the two data points with high M and high crustal thickness results in a nonintuitive negative correlation (r=-0.495, p=0.01), illustrating the weakness of the correlation between *M* and crustal thickness. Thus, while a correlation between *M* and crustal thickness is expected on a global scale—as both are known to increase with increasing spreading rate [e.g., Dick et al., 2003; Olive et al., 2015]—it is possible that our transect did not encounter strong enough fluctuations in magma supply to be clearly reflected in both crustal thickness and tectonic fabric.

6.0 Conclusion:

We conducted one of the longest continuous geophysical surveys along a 1400-km spreading-parallel flow line across the Mid-Atlantic Ridge from 28 Ma on the African Plate to 74 Ma on the North American plate. The transect was analyzed to study co-variability in bathymetry, gravity, and fault statistics in order to elucidate tectono-magmatic variability through time at a single slow-spreading ridge segment. Gravity-derived crustal thickness varies from 3–9 km along the transect with a standard deviation of 1.0 km assuming a mean crustal thickness of 6 km. Admittance and coherence of gravity and bathymetry predict the effective elastic thickness of the lithosphere, T_e, to be 6–12 km, consistent with other estimates for young oceanic lithosphere and indicating that most lithospheric loading that produced relief occurred near, but not on the ridge axis.

Bathymetry and RMBA spectral densities show concurrent peaks on both the eastern and western flanks (0-28 Ma) at 390-, 550-, and 950-kyr periods, with diffuse power at longer periods (>1 Myr). We interpret the diffuse power along the transect as due to a combination of detachment faulting, mantle source heterogeneities (thermal and/or compositional), and variations in upper mantle flow. The 390-kyr spectral peak corresponds to the characteristic spacing of abyssal hill-bounding faults. By contrast, the

550- and 950-kyr peaks are more likely explained by short-wavelength mantle source heterogeneities and/or magma solitons. Further off-axis (28–51 Ma), RMBA spectral density shows a diffuse peak at 650 kyr instead of 550 and 950 kyr could be caused by a change in these tectono-magmatic processes over >10 Myr time periods. Further modelling and analysis are necessary to better quantify the characteristic time scales of these processes and their parameter dependence.

Finally, fault statistics and the identification of a newly observed, off-axis oceanic core complex suggest *M* values ranging from 0.5–0.85 along flow line. We find a significant negative correlation between fault spacing and gravity-derived crustal thickness, indicating the variations in fault spacing along the flow line reflect variability in magmatic input into the brittle crust of the MAR over time. This implies that future statistical analyses of fault populations have the potential to identify variations in mantle melting and melt transport at mid-ocean ridges. In particular, further studies that jointly analyze faulting characteristics and crustal thickness have the potential to elucidate past variations in magma production.

7.0 Acknowledgements:

Data and supplemental materials are available at the Woods Hole Open Access Server (doi.org/10.26025/1912/24796). We would like to thank the Woods Hole Oceanographic Institution, National Science Foundation, Naval Oceanographic Office, and the captain and crew of R/V Neil Armstrong for making the SCARF cruise possible. We would also like to thank Eboné Pierce for her help during the cruise. We thank Meghan Jones for advice using MBSystem. We also thank Maurice Tivey, John Greene, and Masako Tominaga for advice on processing the magnetic datasets. We would like to thank Peter Huybers for sharing his spectral analysis codes. We would like to thank Rob Sohn for his help on interpreting spectral analysis. We would like to thank Del Bohnenstiel, Milena Marjanović, one anonymous reviewer, and Editor Thorsten Becker for their very helpful comments that improved this manuscript. Funding was provided for this research by NSF OCE-14-58201.

References

Ballard, R. D., Bryan, W. B., Heirtzler, J. R., Keller, G., Moore, J. G., & Van Andel, T. (1975). Manned submersible observations in the FAMOUS area: Mid-Atlantic Ridge. Science, 103-108.

Behn, M. D., & Ito, G. (2008). Magmatic and tectonic extension at mid-ocean ridges: 1. Controls on fault characteristics. Geochemistry, Geophysics, Geosystems, 9(8).

Behn, M. D., & Grove, T. L. (2015). Melting systematics in mid-ocean ridge basalts: Application of a plagioclase-spinel melting model to global variations in major element chemistry and crustal thickness. Journal of Geophysical Research: Solid Earth, 120(7), 4863-4886.

Bohnenstiehl, D. R., and S. M. Carbotte (2001), Faulting patterns near 19°30'S on the East Pacific Rise: Faults formation and growth at a superfast spreading center, Geochem. Geophys. Geosyst., 2(9), 1056, doi:10.1029/2001GC000156.

Bohnenstiehl, D. R., and M. C. Kleinrock (1999), Faulting and fault scaling on the median valley floor of the trans-Atlantic geotraverse (TAG) segment, 268N on the Mid-Atlantic Ridge, J. Geophys. Res., 104, 29,351–29,364.

Bonatti, E., Ligi, M., Brunelli, D., Cipriani, A., Fabretti, P., Ferrante, V., ... & Ottolini, L. (2003). Mantle thermal pulses below the Mid-Atlantic Ridge and temporal variations in the formation of oceanic lithosphere. Nature, 423(6939), 499.

Bougault, H., Dmitriev, L., Schilling, J. G., Sobolev, A., Joron, J. L., & Needham, H. D. (1988). Mantle heterogeneity from trace elements: MAR triple junction near 14 N. *Earth and Planetary Science Letters*, 88(1-2), 27-36.

Buck, W. R. (1993). Effect of lithospheric thickness on the formation of high-and low-angle normal faults. Geology, 21(10), 933-936.

Buck, W. R., Lavier, L. L., & Poliakov, A. N. (2005). Modes of faulting at mid-ocean ridges. Nature, 434(7034), 719.

Calmant, S., & Cazenave, A. (1987). Anomalous elastic thickness of the oceanic lithosphere in the south–central Pacific. Nature, 328(6127), 236.

Canales, J. P., Collins, J. A., Escartín, J., & Detrick, R. S. (2000a). Seismic structure across the rift valley of the Mid-Atlantic Ridge at 23 20′(MARK area): Implications for crustal accretion processes at slow spreading ridges. Journal of Geophysical Research: Solid Earth, 105(B12), 28411-28425.

Canales, J. P., Detrick, R. S., Lin, J., Collins, J. A., & Toomey, D. R. (2000b). Crustal and upper mantle seismic structure beneath the rift mountains and across a nontransform offset at the Mid-Atlantic Ridge (35 N). Journal of Geophysical Research: Solid Earth, 105(B2), 2699-2719.

Cann, J. R., Blackman, D. K., Smith, D. K., McAllister, E., Janssen, B., Mello, S., ... & Escartín, J. (1997). Corrugated slip surfaces formed at ridge–transform intersections on the Mid-Atlantic Ridge. Nature, 385(6614), 329.

Cannat, M. (1996). How thick is the magmatic crust at slow spreading oceanic ridges? Journal of Geophysical Research: Solid Earth, 101(B2), 2847-2857.

Carbotte, S. M., and K. C. Macdonald (1994), Comparison of seafloor tectonic fabric at intermediate, fast, and super fast spreading ridges: Influence of spreading rate, plate motions, and ridge segmentation on fault patterns, J. Geophys. Res., 99, 609–613.

Carbotte, S. M., Nedimović, M. R., Canales, J. P., Kent, G. M., Harding, A. J., &

Marjanović, M. (2008). Variable crustal structure along the Juan de Fuca Ridge: Influence of on - axis hot spots and absolute plate motions. Geochemistry, Geophysics, Geosystems, 9(8).

Caress, D. W., Menard, H. W., & Hey, R. N. (1988). Eocene reorganization of the Pacific-Farallon spreading center north of the Mendocino Fracture Zone. Journal of Geophysical Research: Solid Earth, 93(B4), 2813-2838.

Caress, D. W., and D. N. Chayes (2017). MB-System: Mapping the Seafloor. https://www.mbari.org/products/research-software/mb-system.

Chen, Y., & Morgan, W. J. (1990a). Rift valley/no rift valley transition at mid-ocean ridges. Journal of Geophysical Research: Solid Earth, 95(B11), 17571-17581.

Chen, Y., & Morgan, W. J. (1990b). A nonlinear rheology model for mid-ocean ridge axis topography. Journal of Geophysical Research: Solid Earth, 95(B11), 17583-17604.

Chen, Y. J. (1992). Oceanic crustal thickness versus spreading rate. Geophysical Research Letters, 19(8), 753-756.

Cowie, P. A., C. H. Scholz, M. Edwards, and A. Malinverno (1993), Fault strain and seismic coupling on mid-ocean ridges, J. Geophys. Res., 98, 911–917.

Crowley, J. W., Katz, R. F., Huybers, P., Langmuir, C. H., & Park, S. H. (2015). Glacial cycles drive variations in the production of oceanic crust. Science, 347(6227), 1237-1240.

Detrick, R. S., Needham, H. D., & Renard, V. (1995). Gravity anomalies and crustal thickness variations along the Mid-Atlantic Ridge between 33° N and 40° N. Journal of Geophysical Research: Solid Earth, 100(B3), 3767-3787.

Divins, D. L. (2003). Total sediment thickness of the world's oceans & marginal seas. NOAA National Geophysical Data Center, Boulder, CO.

Eason, D. E., Dunn, R. A., Pablo Canales, J., & Sohn, R. A. (2016). Segment - scale variations in seafloor volcanic and tectonic processes from multibeam sonar imaging, Mid-Atlantic Ridge Rainbow region (35° 45'–36° 35'N). Geochemistry, Geophysics, Geosystems, 17(9), 3560-3579.

Escartín, J., Cannat, M., Pouliquen, G., Rabain, A., & Lin, J. (2001). Crustal thickness of V-shaped ridges south of the Azores: Interaction of the Mid-Atlantic Ridge (36–39 N) and the Azores hot spot. Journal of Geophysical Research: Solid Earth, 106(B10), 21719-21735.

Escartín, J., Smith, D. K., Cann, J., Schouten, H., Langmuir, C. H., & Escrig, S. (2008). Central role of detachment faults in accretion of slow-spreading oceanic lithosphere. Nature, 455(7214), 790.

Escartín, J., Mevel, C., Petersen, S., Bonnemains, D., Cannat, M., Andreani, M., ... & Godard, M. (2017). Tectonic structure, evolution, and the nature of oceanic core complexes and their detachment fault zones (13 20' N and 13 30' N, Mid Atlantic Ridge). Geochemistry, Geophysics, Geosystems, 18(4), 1451-1482.

Elliott, T., & Spiegelman, M. (2003). Melt migration in oceanic crustal production: a U-series perspective. Treatise on geochemistry, 3, 659.

Ferguson, D. J., Li, Y., Langmuir, C. H., Costa, K. M., McManus, J. F., Huybers, P., & Carbotte, S. M. (2017). A 65 ky time series from sediment-hosted glasses reveals rapid transitions in ocean ridge magmas. Geology, 45(6), 491-494.

Finlay, C. C., Maus, S., Beggan, C. D., Bondar, T. N., Chambodut, A., Chernova, T. A.,

... & Holme, R. (2010). International geomagnetic reference field: the eleventh generation. *Geophysical Journal International*, 183(3), 1216-1230.

Forsyth, D. W. (1985). Subsurface loading and estimates of the flexural rigidity of continental lithosphere. *Journal of Geophysical Research: Solid Earth*, 90(B14), 12623-12632.

Forsyth, D. W. (1992). Finite extension and low-angle normal faulting. Geology, 20(1), 27-30.

Gale, A., Dalton, C. A., Langmuir, C. H., Su, Y., & Schilling, J. G. (2013). The mean composition of ocean ridge basalts. Geochemistry, Geophysics, Geosystems, 14(3), 489-518.

German, C. R., Klinkhammer, G. P., & Rudnicki, M. D. (1996). The Rainbow hydrothermal plume, 36˚15'N, MAR. Geophysical Research Letters, 23(21), 2979-2982.

Goff, J. A. (2015). Comment on "Glacial cycles drive variations in the production of oceanic crust". Science, 349(6252), 1065-1065.

Goff, J. A., Zahirovic, S., & Müller, R. D. (2018). No Evidence for Milankovitch Cycle Influence on Abyssal Hills at Intermediate, Fast, and Superfast Spreading Rates. Geophysical Research Letters, 45(19), 10-305.

Hamilton, E. L. (1978). Sound velocity–density relations in sea‐floor sediments and rocks. *The Journal of the Acoustical Society of America*, 63(2), 366-377.

Hayman, N. W., Grindlay, N. R., Perfit, M. R., Mann, P., Leroy, S., & de Lépinay, B. M. (2011). Oceanic core complex development at the ultraslow spreading Mid‐Cayman Spreading Center. Geochemistry, Geophysics, Geosystems, 12(3).

Hooft, E. E. E., R. S. Detrick, D. R. Toomey, J. A. Collins, & J. Lin (2000). Crustal thickness and structure along three contrasting spreading segments of the Mid-Atlantic Ridge, 33.5°–35°N, J. Geophys. Res., 105, 8205–8226, doi:10.1029/1999JB900442.

Howell, S. M., Ito, G., Behn, M. D., Martinez, F., Olive, J. A., & Escartín, J. (2016). Magmatic and tectonic extension at the Chile Ridge: Evidence for mantle controls on ridge segmentation. Geochemistry, Geophysics, Geosystems, 17(6), 2354-2373.

Howell, S. M., Olive, J. A., Ito, G., Behn, M. D., Escartín, J., & Kaus, B. (2019). Seafloor expression of oceanic detachment faulting reflects gradients in mid-ocean ridge magma supply. Earth and Planetary Science Letters, 516, 176-189.

Ito, G., & Behn, M. D. (2008). Magmatic and tectonic extension at mid‐ocean ridges: 2. Origin of axial morphology. Geochemistry, Geophysics, Geosystems, 9(9).

Jourdan, F., Marzoli, A., Bertrand, H., Cirilli, S., Tanner, L. H., Kontak, D. J., ... & Bellieni, G. (2009). 40Ar/39Ar ages of CAMP in North America: implications for the Triassic–Jurassic boundary and the 40K decay constant bias. Lithos, 110(1-4), 167-180.

Katz, R. F., & Weatherley, S. M. (2012). Consequences of mantle heterogeneity for melt extraction at mid-ocean ridges. Earth and Planetary Science Letters, 335, 226-237.

Kleinrock, M. C., Tucholke, B. E., Lin, J., & Tivey, M. A. (1997). Fast rift propagation at a slow-spreading ridge. *Geology*, 25(7), 639-642.

Kuo, B. Y., & Forsyth, D. W. (1988). Gravity anomalies of the ridge-transform system in the South Atlantic between 31 and 34.5 S: Upwelling centers and variations in crustal thickness. Marine Geophysical Researches, 10(3-4), 205-232.

Labails, C., Olivet, J. L., Aslanian, D., & Roest, W. R. (2010). An alternative early opening scenario for the Central Atlantic Ocean. *Earth and Planetary Science Letters*, 297(3-4), 355-368.

Langmuir, C. H., Klein, E. M., & Plank, T. (1992). Petrological systematics of mid-ocean ridge basalts: Constraints on melt generation beneath ocean ridges. Mantle flow and melt generation at mid-ocean ridges, 71, 183-280.

Liu, Z., & Buck, W. R. (2018). Magmatic controls on axial relief and faulting at mid-ocean ridges. *Earth and Planetary Science Letters*, 491, 226-237.

Lin, J., Purdy, G. M., Schouten, H., Sempere, J. C., & Zervas, C. (1990). Evidence from gravity data for focused magmatic accretion along the Mid-Atlantic Ridge. Nature, 344(6267), 627.

Lizarralde, D., Gaherty, J. B., Collins, J. A., Hirth, G., & Kim, S. D. (2004). Spreading-rate dependence of melt extraction at mid-ocean ridges from mantle seismic refraction data. Nature, 432(7018), 744.

Macdonald, K. C., Fox, P. J., Alexander, R. T., Pockalny, R., & Gente, P. (1996). Volcanic growth faults and the origin of Pacific abyssal hills. Nature, 380(6570), 125.

MacLeod, C. J., Searle, R. C., Murton, B. J., Casey, J. F., Mallows, C., Unsworth, S. C., ... & Harris, M. (2009). Life cycle of oceanic core complexes. Earth and Planetary Science Letters, 287(3-4), 333-344.

McKenzie, D. (1985). The extraction of magma from the crust and mantle. Earth and Planetary Science Letters, 74(1), 81-91.

McNutt, M. K. (1984). Lithospheric flexure and thermal anomalies. Journal of Geophysical Research: Solid Earth, 89(B13), 11180-11194.

Meyer, B., Saltus, R., & Chulliat, A. (2016). EMAG2: Earth magnetic anomaly grid (2 - arc - minute resolution) version 3. National Centers for Environmental Information, NOAA. Model. https://doi.org/10.7289/V5H70CVX

Minshull, T. A., Muller, M. R., & White, R. S. (2006). Crustal structure of the Southwest Indian Ridge at 66 E: Seismic constraints. Geophysical Journal International, 166(1), 135-147.

Montési, L. G. J., & Behn, M. D. (2007). Mantle flow and melting underneath oblique and ultraslow mid-ocean ridges. Geophysical Research Letters, 34(24).

Moritz, H. (1980). Geodetic reference system 1980. Journal of Geodesy, 54(3), 395-405.

Morris, E., Detrick, R. S., Minshull, T. A., Mutter, J. C., White, R. S., Su, W., & Buhl, P. (1993). Seismic structure of oceanic crust in the western North Atlantic. Journal of Geophysical Research: Solid Earth, 98(B8), 13879-13903.

Müller, R. D., Sdrolias, M., Gaina, C., & Roest, W. R. (2008). Age, spreading rates, and spreading asymmetry of the world's ocean crust. Geochemistry, Geophysics, Geosystems, 9(4).

Nicolas, A., Boudier, F., & Ildefonse, B. (1996). Variable crustal thickness in the Oman ophiolite: implication for oceanic crust. *Journal of Geophysical Research: Solid Earth*, 101(B8), 17941-17950.

Olive, J. A., Behn, M. D., & Tucholke, B. E. (2010). The structure of oceanic core complexes controlled by the depth distribution of magma emplacement. *Nature Geoscience*, 3(7), 491.

Olive, J. A., Behn, M. D., Ito, G., Buck, W. R., Escartín, J., & Howell, S. (2015). Sensitivity of seafloor bathymetry to climate-driven fluctuations in mid-ocean ridge magma supply. Science, 350(6258), 310-313.

Olive, J.-A., Behn, M. D., Ito, G., Buck, W. R., Escartín, J., & Howell, S. (2016). Response to comment on "Sensitivity of seafloor bathymetry to climate-driven fluctuations in mid-ocean ridge magma supply.". Science, 352(6292), 1405-c.

Pariso, J. E., Sempéré, J. C., & Rommevaux, C. (1995). Temporal and spatial variations in crustal accretion along the Mid‐Atlantic Ridge (29°–31° 30′ N) over the last 10 my: Implications from a three‐dimensional gravity study. Journal of Geophysical Research: Solid Earth, 100(B9), 17781-17794.

Parker, R. L. (1972) The rapid calculation of potential anomalies. Geophys. J. R. Astr. Soc., 3, pp. 447-455

Parmentier, E. M., & Morgant, J. P. (1990). Spreading rate dependence of three-dimensional structure in oceanic spreading centres. Nature, 348(6299), 325.

Parnell-Turner, R., Escartín, J., Olive, J. A., Smith, D. K., & Petersen, S. (2018). Genesis of corrugated fault surfaces by strain localization recorded at oceanic detachments. Earth and Planetary Science Letters, 498, 116-128.

Paulatto, M., Canales, J. P., Dunn, R. A., & Sohn, R. A. (2015). Heterogeneous and asymmetric crustal accretion: New constraints from multibeam bathymetry and potential field data from the Rainbow area of the Mid-Atlantic Ridge (36° 15'N). Geochemistry, Geophysics, Geosystems, 16(9), 2994-3014.

Percival, D., and A. Walden (1993) Spectral Analysis for Physical Applications: Multitaper and Conventional Univariate Techniques Cambridge University Press

Purdy, G. M., Kong, L. S. L., Christeson, G. L., & Solomon, S. C. (1992). Relationship between spreading rate and the seismic structure of mid-ocean ridges. *Nature*, 355(6363), 815.

Roth, S., Granot, R., & Downey, N. J. (2019). Discrete characterization of abyssal hills: Unraveling temporal variations in crustal accretion processes at the 10° 30′ N segment, East Pacific Rise. Earth and Planetary Science Letters, 525, 115762.

Rubin, A. M., & Pollard, D. D. (1988). Dike-induced faulting in rift zones of Iceland and Afar. Geology, 16(5), 413-417.

Sandwell, D. T., R. D. Müller, W. H. F. Smith, E. Garcia, R. Francis, New global marine gravity model from CryoSat-2 and Jason-1 reveals buried tectonic structure, Science, Vol. 346, no. 6205, pp. 65-67, doi: 10.1126/science.1258213, 2014.

Schettino, A., & Scotese, C. R. (2005). Apparent polar wander paths for the major continents (200 Ma to the present day): a palaeomagnetic reference frame for global plate tectonic reconstructions. *Geophysical Journal International*, 163(2), 727-759.

Schettino, A. (2014). Quantitative plate tectonics. *Physics of the Earth–Plate Kinematics–Geodynamics.*

Schouten, H., & Klitgord, K. D. (1982). The memory of the accreting plate boundary and the continuity of fracture zones. *Earth and Planetary Science Letters*, *59*(2), 255-266.

Schouten, H., Smith, D. K., Cann, J. R., & Escartín, J. (2010). Tectonic versus magmatic extension in the presence of core complexes at slow-spreading ridges from a visualization of faulted seafloor topography. Geology, 38(7), 615-618.

Scott, D. R., & Stevenson, D. J. (1984). Magma solitons. Geophysical Research Letters, 11(11), 1161-1164.

Searle, R. (2013). Mid-ocean ridges. Cambridge University Press.

Seher, T., Crawford, W. C., Singh, S. C., Cannat, M., Combier, V., & Dusunur, D. (2010). Crustal velocity structure of the Lucky Strike segment of the Mid-Atlantic Ridge at 37 N from seismic refraction measurements. Journal of Geophysical Research: Solid Earth, 115(B3).

Seton, M., Müller, R. D., Zahirovic, S., Gaina, C., Torsvik, T., Shephard, G., ... & Chandler, M. (2012). Global continental and ocean basin reconstructions since 200 Ma. Earth-Science Reviews, 113(3-4), 212-270.

Shaw, P. R. (1992). Ridge segmentation, faulting and crustal thickness in the Atlantic Ocean. *Nature*, 358(6386), 490.

Shaw, P. R., & Lin, J. (1993). Causes and consequences of variations in faulting style at the Mid‐Atlantic Ridge. *Journal of Geophysical Research: Solid Earth*, 98(B12), 21839-21851.

Shirey, S. B., Bender, J. F., & Langmuir, C. H. (1987). Three-component isotopic heterogeneity near the Oceanographer transform, Mid-Atlantic Ridge. *Nature*, 325(6101), 217.

Sinton, J. M., & Detrick, R. S. (1992). Mid‐ocean ridge magma chambers. Journal of Geophysical Research: Solid Earth, 97(B1), 197-216.

Sim, S. J., Spiegelman, M. W., Stegman, D. R., & Wilson, C. R. (2018, December). Melt focusing at mid ocean ridges. In AGU Fall Meeting Abstracts, Abstract DI43C-0045.

Smith, D. K., Escartín, J., Schouten, H., & Cann, J. R. (2008). Fault rotation and core complex formation: Significant processes in seafloor formation at slow‐spreading mid‐ocean ridges (Mid‐Atlantic Ridge, 13–15 N). *Geochemistry, Geophysics, Geosystems*, 9(3).

Spearman, C. (1904). The proof and measurement of association between two things. American Journal of Psychology, 15(1), 72-101.

Tan, Y. J., Tolstoy, M., Waldhauser, F., & Wilcock, W. S. (2016). Dynamics of a seafloor-spreading episode at the East Pacific Rise. Nature, 540(7632), 261.

Tivey, M. A., & Tucholke, B. E. (1998). Magnetization of 0–29 Ma ocean crust on the Mid‐Atlantic Ridge, 25° 30′ to 27° 10′ N. Journal of Geophysical Research: Solid Earth, 103(B8), 17807-17826.

Tolstoy, M. (2015). Mid-ocean ridge eruptions as a climate valve. Geophysical Research Letters, 42(5), 1346-1351.

Tolstoy, M., Harding, A. J., & Orcutt, J. A. (1993). Crustal thickness on the Mid-Atlantic Ridge: Bull's-eye gravity anomalies and focused accretion. Science, 262(5134), 726-729.

Tucholke, B. E., Lin, J., Kleinrock, M. C., Tivey, M. A., Reed, T. B., Goff, J., & Jaroslow, G. E. (1997). Segmentation and crustal structure of the western Mid-Atlantic Ridge flank, 25° 25′–27° 10′ N and 0–29 my. Journal of Geophysical Research: Solid Earth, 102(B5), 10203-10223.

Tucholke, B. E., Lin, J., & Kleinrock, M. C. (1998). Megamullions and mullion structure defining oceanic metamorphic core complexes on the Mid‐Atlantic Ridge. *Journal of Geophysical Research: Solid Earth*, 103(B5), 9857-9866.

Tucholke, B. E., Behn, M. D., Buck, W. R., & Lin, J. (2008). Role of melt supply in oceanic detachment faulting and formation of megamullions. Geology, 36(6), 455-458.

Turcotte, D., & Schubert, G. (2014). *Geodynamics*. Cambridge University Press.

Wang, T., Lin, J., Tucholke, B., & Chen, Y. J. (2011). Crustal thickness anomalies in the North Atlantic Ocean basin from gravity analysis. *Geochemistry, Geophysics, Geosystems*, 12(3).

Watts, A. B., Bodine, J. H., & Steckler, M. S. (1980). Observations of flexure and the state of stress in the oceanic lithosphere. Journal of Geophysical Research: Solid Earth, 85(B11), 6369-6376.

Watts, A. B. (2001). Isostasy and Flexure of the Lithosphere. Cambridge University Press.

Weatherall, P., Marks, K. M., Jakobsson, M., Schmitt, T., Tani, S., Arndt, J. E., ... & Wigley, R. (2015). A new digital bathymetric model of the world's oceans. Earth and Space Science, 2(8), 331-345.

Wei, W. (1995). Revised age calibration points for the geomagnetic polarity time scale. Geophysical Research Letters, 22(8), 957-960.

Wessel, P., Smith, W. H., Scharroo, R., Luis, J., & Wobbe, F. (2013). Generic mapping tools: improved version released. Eos, Transactions American Geophysical Union, 94(45), 409-410.

White, W. M., & Schilling, J. G. (1978). The nature and origin of geochemical variation in Mid-Atlantic Ridge basalts from the central North Atlantic. Geochimica et Cosmochimica Acta, 42(10), 1501-1516.

Figure Captions:

Figure 1: Comparison of shipboard and regional data sets along the SCARF cruise track. **a)** Track line bathymetry (scale in km is shown by white bar) plotted along the track line (straight black line) over satellite-derived bathymetry (Weatherall et al., 2015) for the region. The inset shows global plate boundaries (black lines) and our track line (red line). **b)** Shipboard magnetic anomaly (scale in nT is shown by white bar) plotted along the track line over global magnetic anomaly grid EMAG2v3 (Meyer et al., 2016). White lines are other shipboard magnetic anomaly tracks from NCEI’s Marine Trackline Geophysical database (https://www.ngdc.noaa.gov/mgg/geodas/trackline.html). **c)** Shipboard free air gravity anomaly (scale in mGal is shown by white bar) plotted along the track line against 1 arcminute satellite-derived global free air anomaly version 24 (Sandwell et al., 2014).

Figure 2: Comparison of the observed magnetic anomaly along the SCARF transect (blue line) and synthetic magnetic anomaly (black line) calculated from the magnetostratigraphic scale plotted on the bottom. See section 3.1 for synthetic calculation

method. Synthetic profile is vertically translated by -700 nT for illustration purposes. Isochron picks are labeled and represented as dashed grey lines.

Figure 3: Shipboard geophysical datasets and derived geophysical parameters along the SCARF transect. **a)** Track line bathymetry (black) with picked fault locations (red dots, displayed 1 km shallower than picked location). The location of the observed oceanic core complex, Kafka Dome is marked by the blue star, displayed 0.7 km deeper than the picked location. **b)** Binned fault spacing (open circles) and interpolated sediment thickness from compiled isopach maps, ocean drilling records, and seismic reflection data (red line; Divins, 2003). Grey regions denote potential oceanic core complex regimes located symmetrically across the ridge axis. **c)** *M* (circles) calculated as described in Section 3.2. **d)** Half spreading rates calculated from our magnetic anomaly derived ages (black line) and from an interpolated global age grid (Müller et al., 2008). **e)** Calculated residual mantle Bouguer anomaly (RMBA). **f)** Downward continued crustal thickness variations calculated from the RMBA assuming an average crustal thickness of 6 km.

Figure 4: Cumulative frequency distribution of fault throw for the entire SCARF transect (solid black line), as well as for only those faults within 200 km (blue) and 400 km (red) of the ridge axis. The throw distribution from near-ridge picked faults on the Chile Ridge (dashed black line) is shown for comparison. Straight lines in this plot indicate an exponential fault distribution, which is predicted for natural normal fault populations (see Section 3.2). We interpret the difference in the fault population between those located within 400 km of the ridge to that calculated for the entire transect to be due to the increasing effects of sedimentation and mass wasting. Thus, we limit our interpretations to fault statistics within 400 km. The change in slope of the fault distributions for throws > 0.6 km is likely due to the low number of observed high throw faults in our dataset.

Figure 5: a) Shaded bathymetry for our observed oceanic core complex, Kafka Dome. White line denotes the ship track. **b)** Calculated RMBA along the track line showing an 8 mGal local increase over the Kafka Dome, characteristic of many oceanic core complexes. **c)** Bathymetry from oceanic core complex 13˚20’ N (Escartín et al., 2017) for comparison. The horizontal scale is the same in both a) and c).

Figure 6: a) Track line bathymetry separated into four sections. **b)** Power spectral density of pre-whitened bathymetry for the three colored sections. **c)** Calculated residual mantle Bouguer anomaly (RMBA) separated into the same sections. **d)** Power spectral density of pre-whitened RMBA. The approximate 5th to 95th percentile confidence interval from the spectral method is indicated by the bottom and top of the black bar in the upper right corner of b) and d) relative to a given value (circle). Vertical dashed lines show interpreted concurrent peaks between the east (red) and the near-axis west (blue) at 390-, 550-, and 950-kyr periods. Dash-dotted line in d) shows the interpreted diffuse peak at 650 kyr for the 28–51 Ma west flank RMBA. Off-axis data shows a different RMBA and bathymetry spectrum compared to the near ridge data.

Figure 7: a) Calculated admittance (black line) plotted alongside theoretical admittance curves for different values of effective elastic thickness, T_e. **b)** Calculated coherence

(black line) plotted alongside theoretical coherence curves for various values of T_e. Both models predict T_e values between 6–12 km.

Figure 8: Schematic diagram depicting potential causes for oceanic crustal thickness variation discussed in Section 5.1.

Figure 9: a) Binned fault spacing versus binned crustal thickness for all bins less than 400 km from the ridge. **b)** Binned crustal thickness against *M* for all bins within 400 km of the ridge. Overlapping bins are 100 km wide every 25 km.

Figure 1.

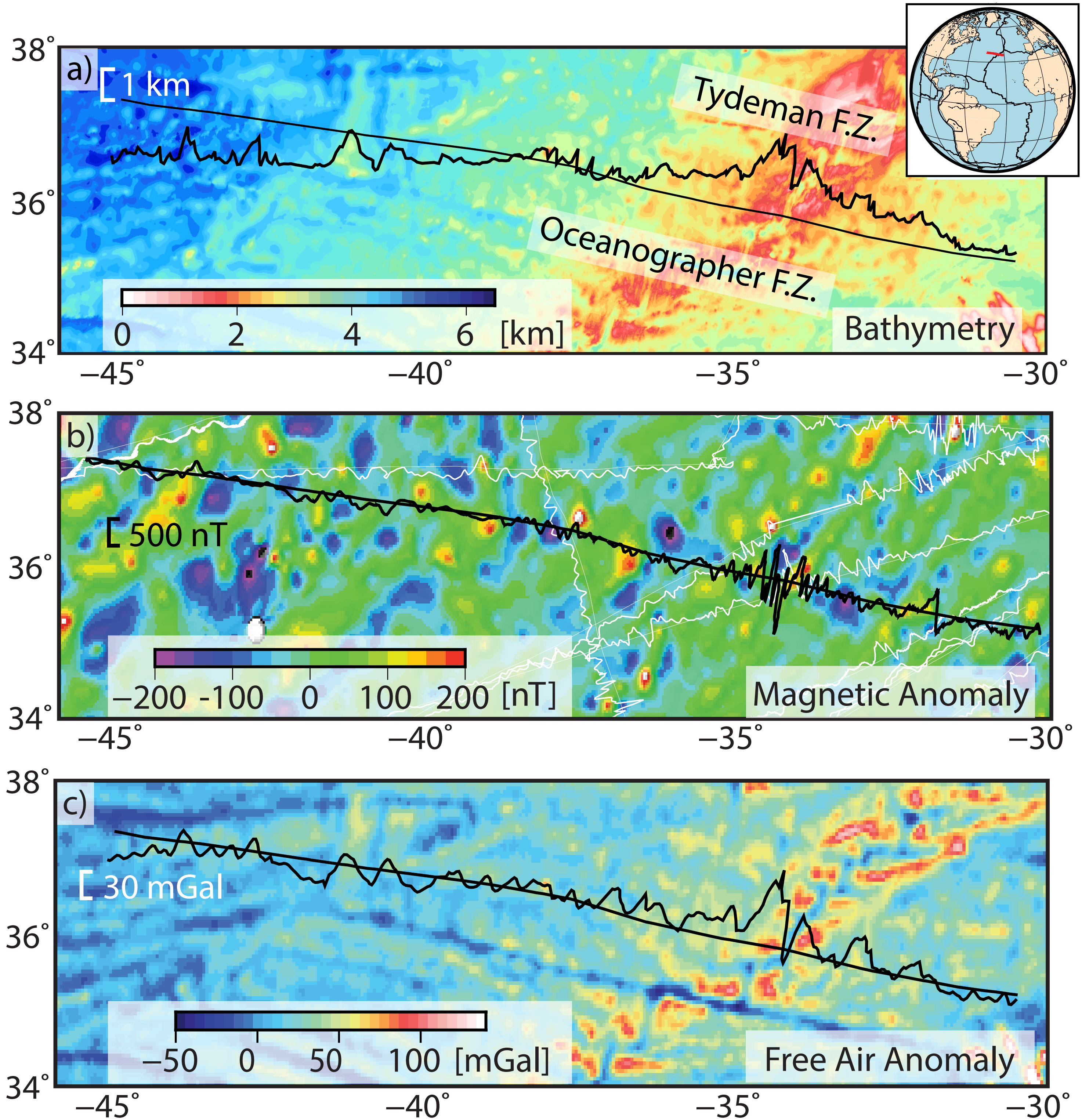
a)
1 km
Tydeman F.Z.
Oceanographer F.Z.
0
2
4
6
[km]
Bathymetry
38°
36°
34°
−45°
−40°
−35°
−30°
b)
500 nT
−200
-100
0
100
200
[nT]
Magnetic Anomaly
38°
36°
34°
−45°
−40°
−35°
−30°
c)
30 mGal
−50
0
50
100
[mGal]
Free Air Anomaly
38°
36°
34°
−45°
−40°
−35°
−30°

Figure 2.

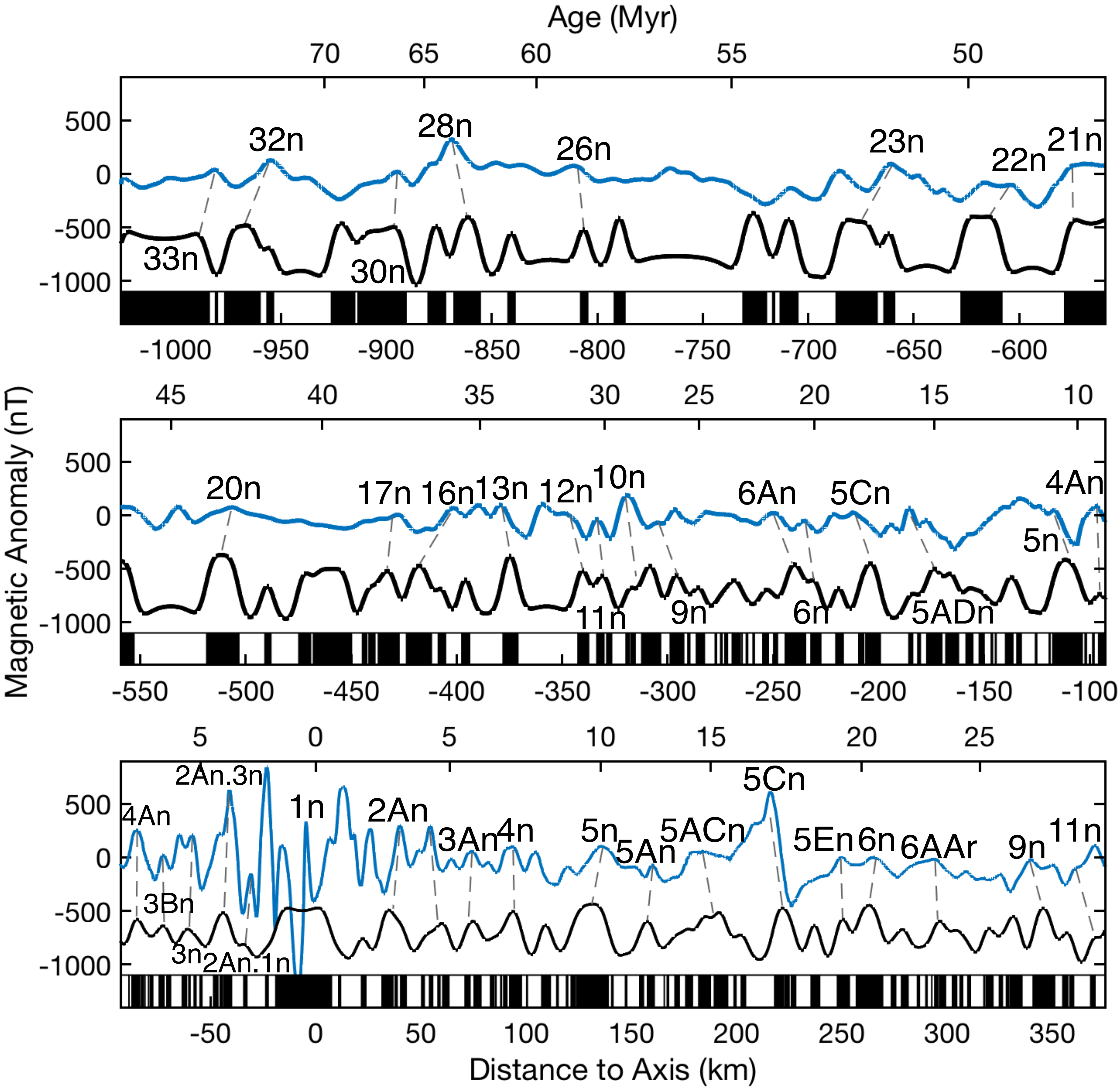

Age (Myr)
Magnetic Anomaly (nT)
Distance to Axis (km)
32n
28n
26n
23n
22n
21n
33n
30n
20n
17n
16n
13n
12n
10n
6An
5Cn
4An
5n
11n
9n
6n
5ADn
2An.3n
4An
1n
2An
3An
4n
5n
5An
5ACn
5Cn
5En
6n
6AAr
9n
11n
3Bn
3n
2An.1n

Figure 3.

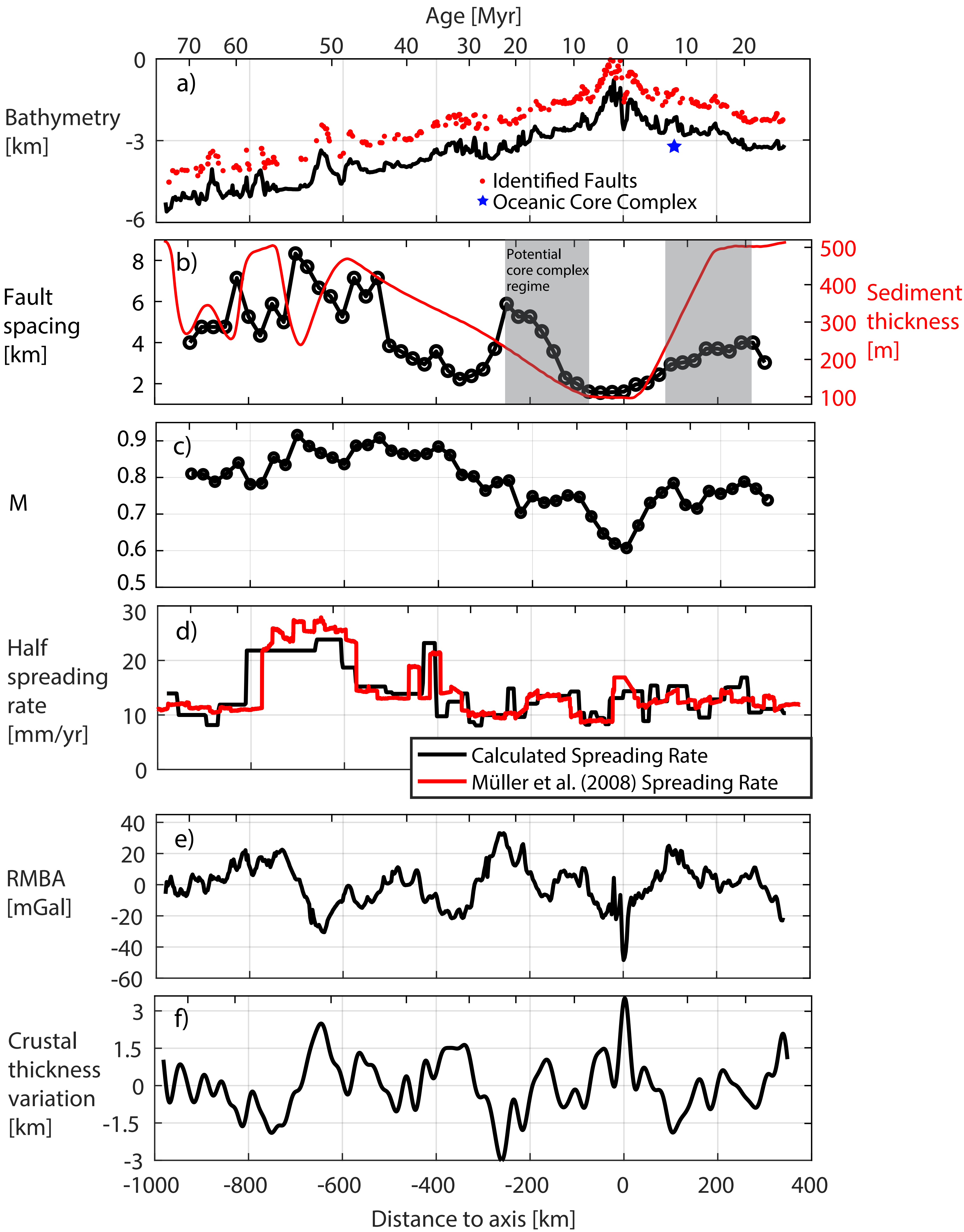

Age [Myr]
70 60 50 40 30 20 10 0 10 20
a)
Bathymetry [km]
0
-3
-6
Identified Faults
Oceanic Core Complex
b)
Fault spacing [km]
8
6
4
2
Potential core complex regime
500
400
300
200
100
Sediment thickness [m]
c)
M
0.9
0.8
0.7
0.6
0.5
d)
Half spreading rate [mm/yr]
30
20
10
0
Calculated Spreading Rate
Müller et al. (2008) Spreading Rate
e)
RMBA [mGal]
40
20
0
-20
-40
-60
f)
Crustal thickness variation [km]
3
1.5
0
-1.5
-3
-1000 -800 -600 -400 -200 0 200 400
Distance to axis [km]

Figure 4.

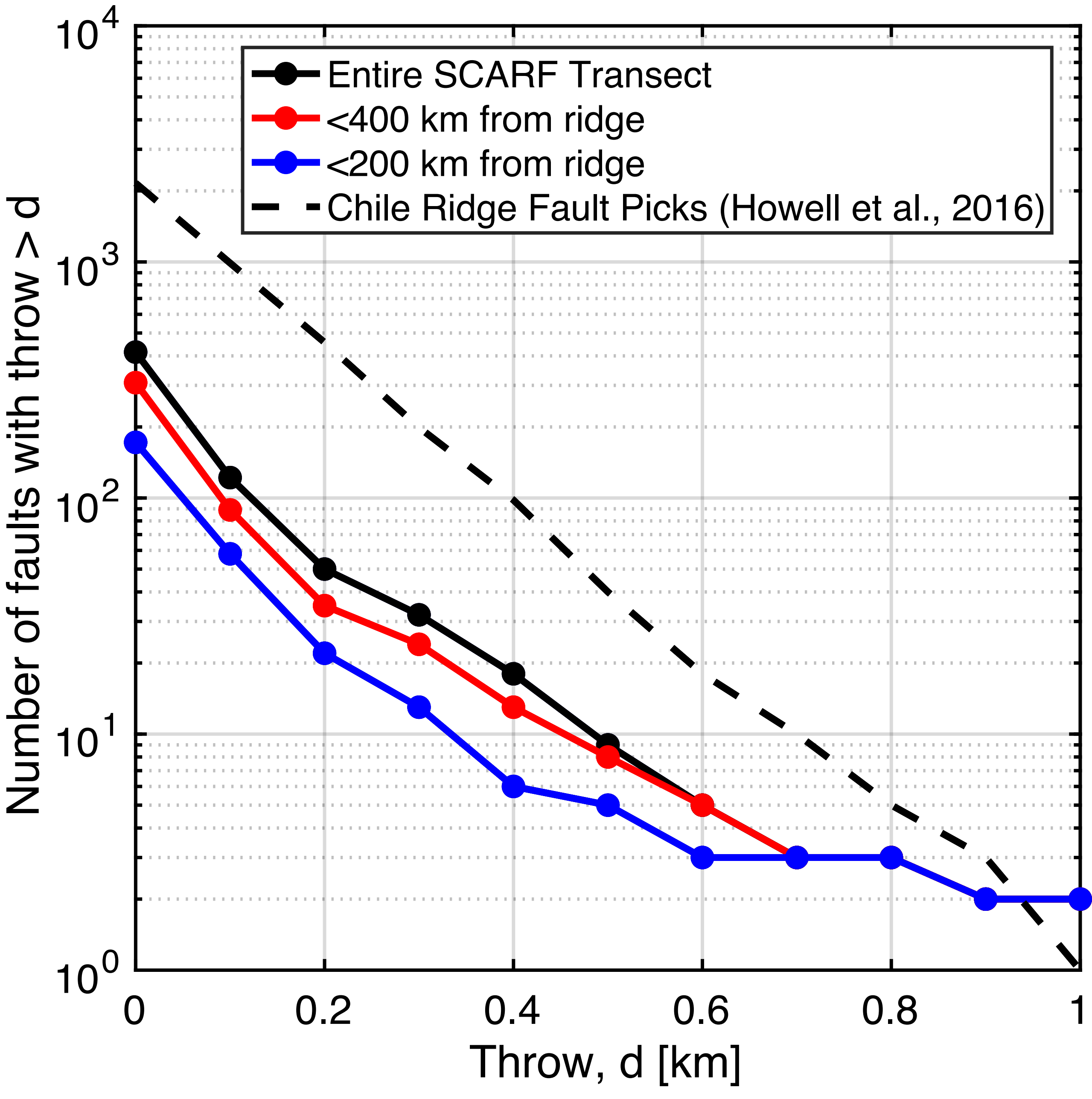
Entire SCARF Transect
<400 km from ridge
<200 km from ridge
Chile Ridge Fault Picks (Howell et al., 2016)
Number of faults with throw > d
Throw, d [km]
10^0
10^1
10^2
10^3
10^4
0
0.2
0.4
0.6
0.8
1

Figure 5.

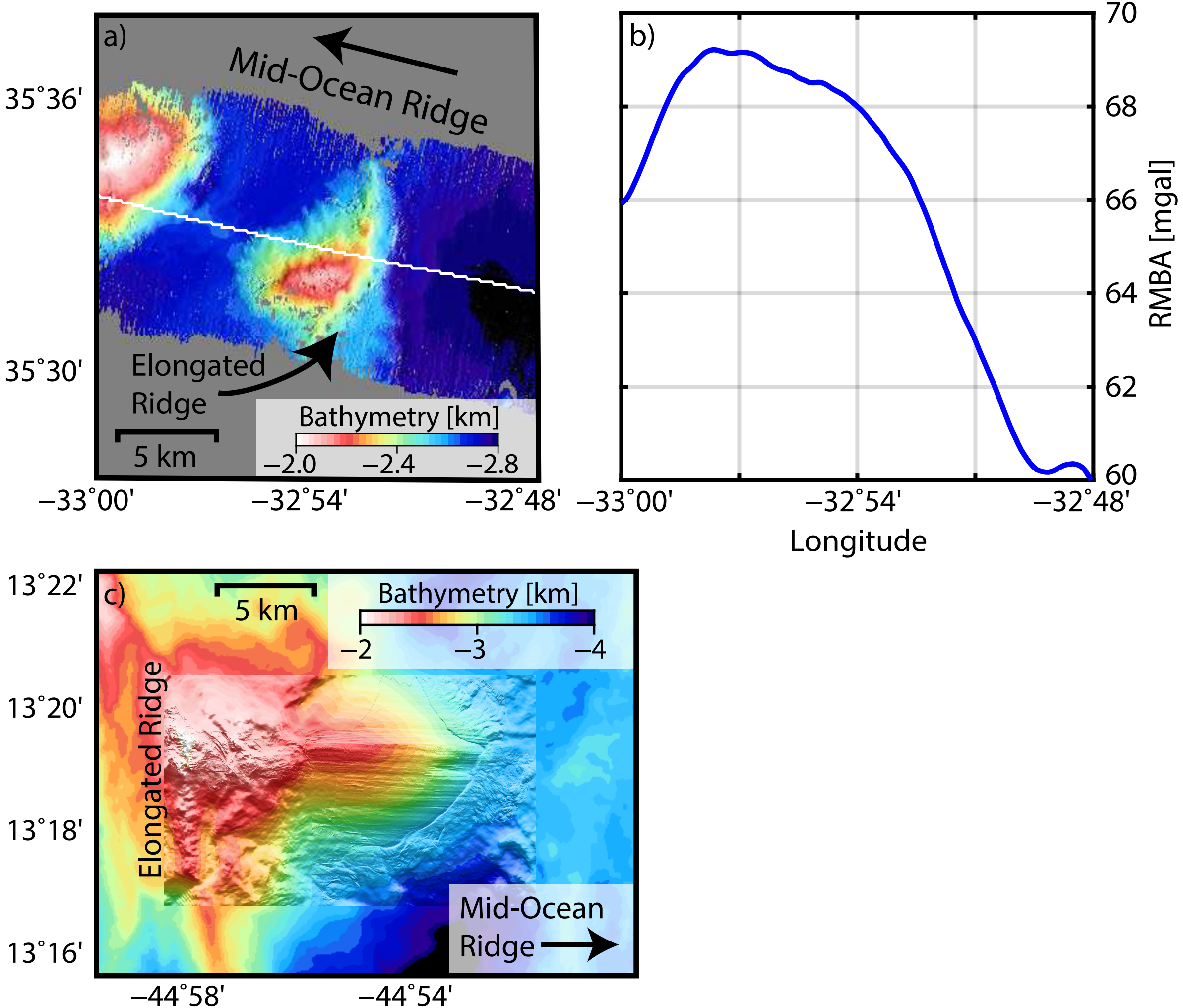

a)
Mid-Ocean Ridge
Elongated Ridge
5 km
Bathymetry [km]
−2.0
−2.4
−2.8
35°36'
35°30'
−33°00'
−32°54'
−32°48'
b)
RMBA [mgal]
70
68
66
64
62
60
−33°00'
−32°54'
−32°48'
Longitude
c)
5 km
Bathymetry [km]
−2
−3
−4
Elongated Ridge
Mid-Ocean Ridge
13°22'
13°20'
13°18'
13°16'
−44°58'
−44°54'

Figure 6.

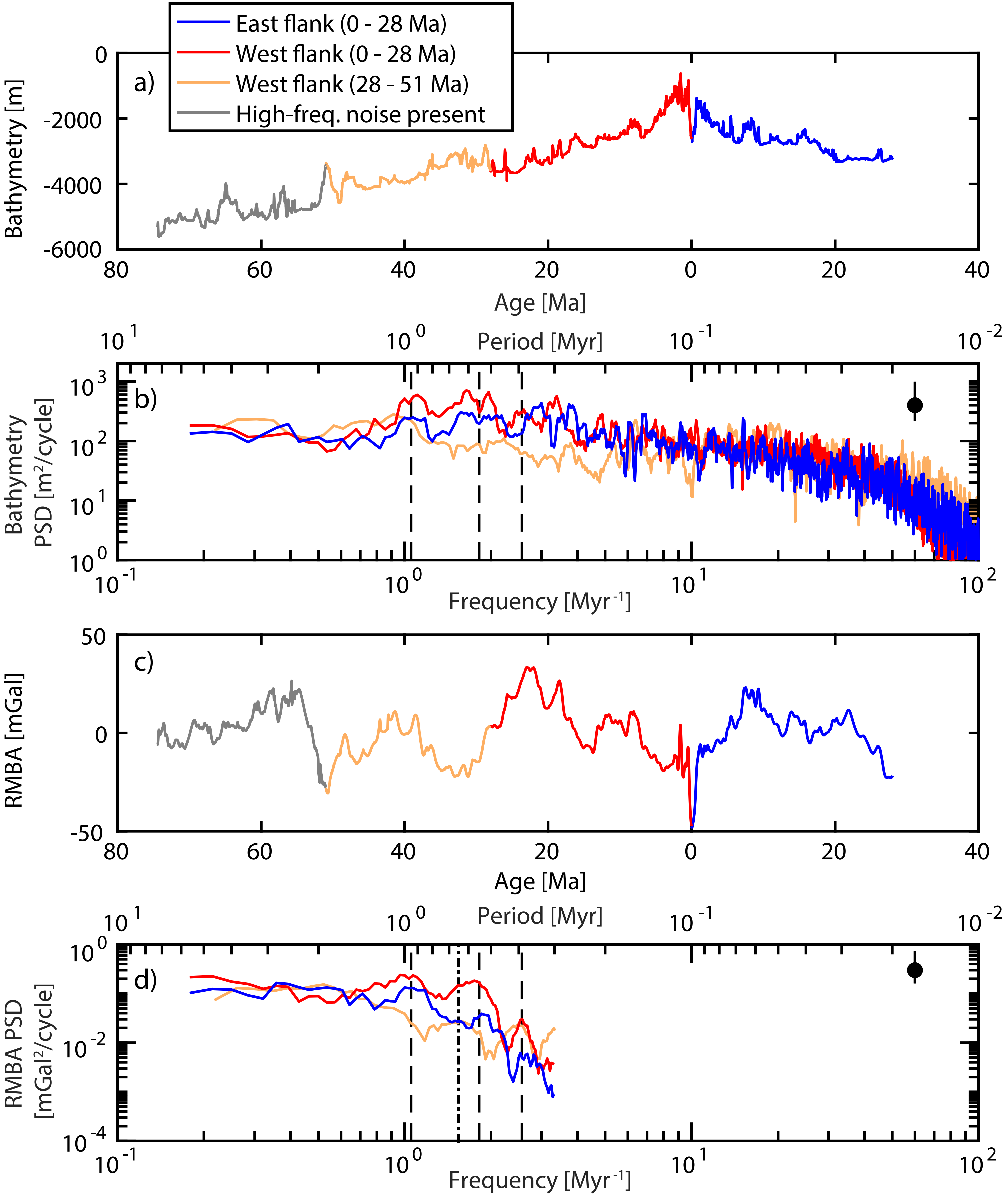
East flank (0 - 28 Ma)
West flank (0 - 28 Ma)
West flank (28 - 51 Ma)
High-freq. noise present
a)
Bathymetry [m]
Age [Ma]
b)
Period [Myr]
Bathymetry PSD [m²/cycle]
Frequency [Myr⁻¹]
c)
RMBA [mGal]
Age [Ma]
d)
Period [Myr]
RMBA PSD [mGal²/cycle]
Frequency [Myr⁻¹]

Figure 7.

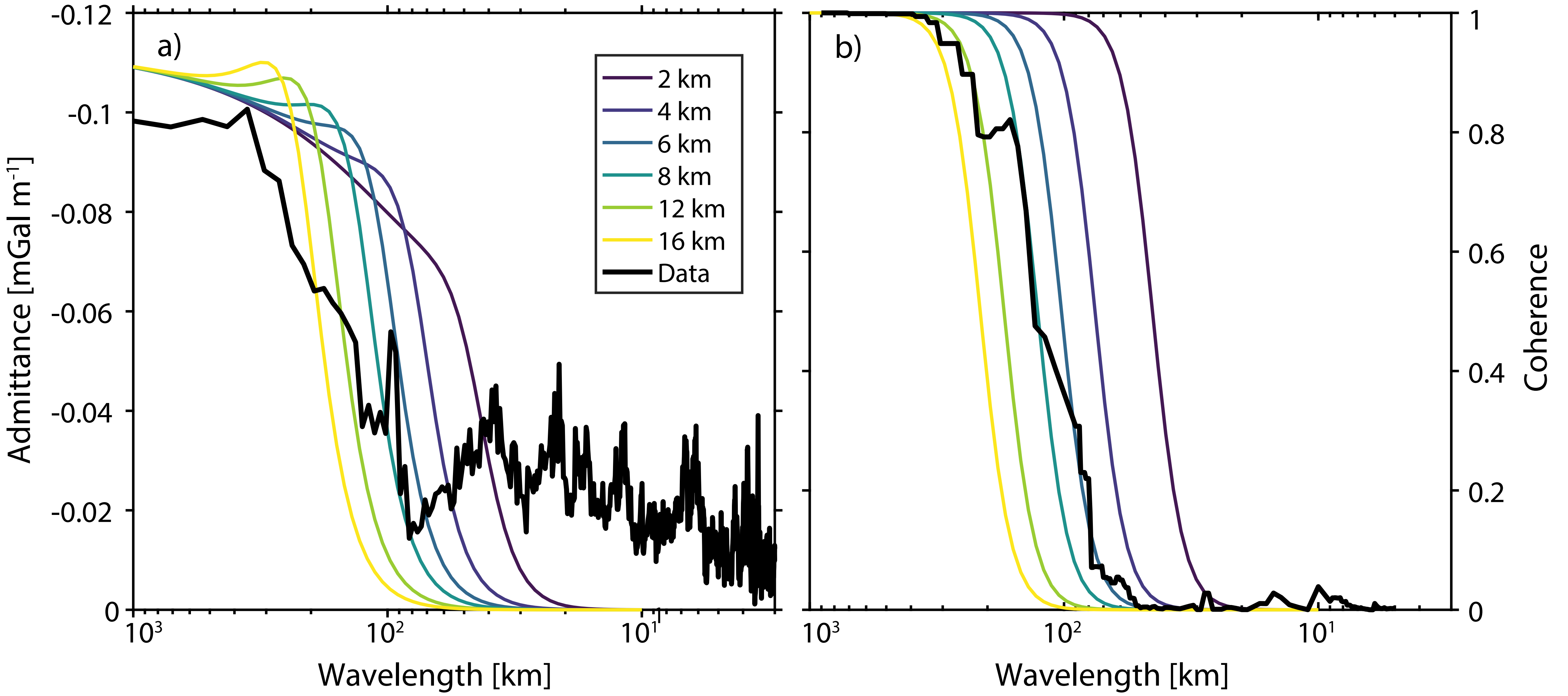

a)
b)
2 km
4 km
6 km
8 km
12 km
16 km
Data
Admittance [mGal m^-1]
Coherence
Wavelength [km]
Wavelength [km]
-0.12
-0.1
-0.08
-0.06
-0.04
-0.02
0
1
0.8
0.6
0.4
0.2
0
10^3
10^2
10^1
10^3
10^2
10^1

Figure 8.

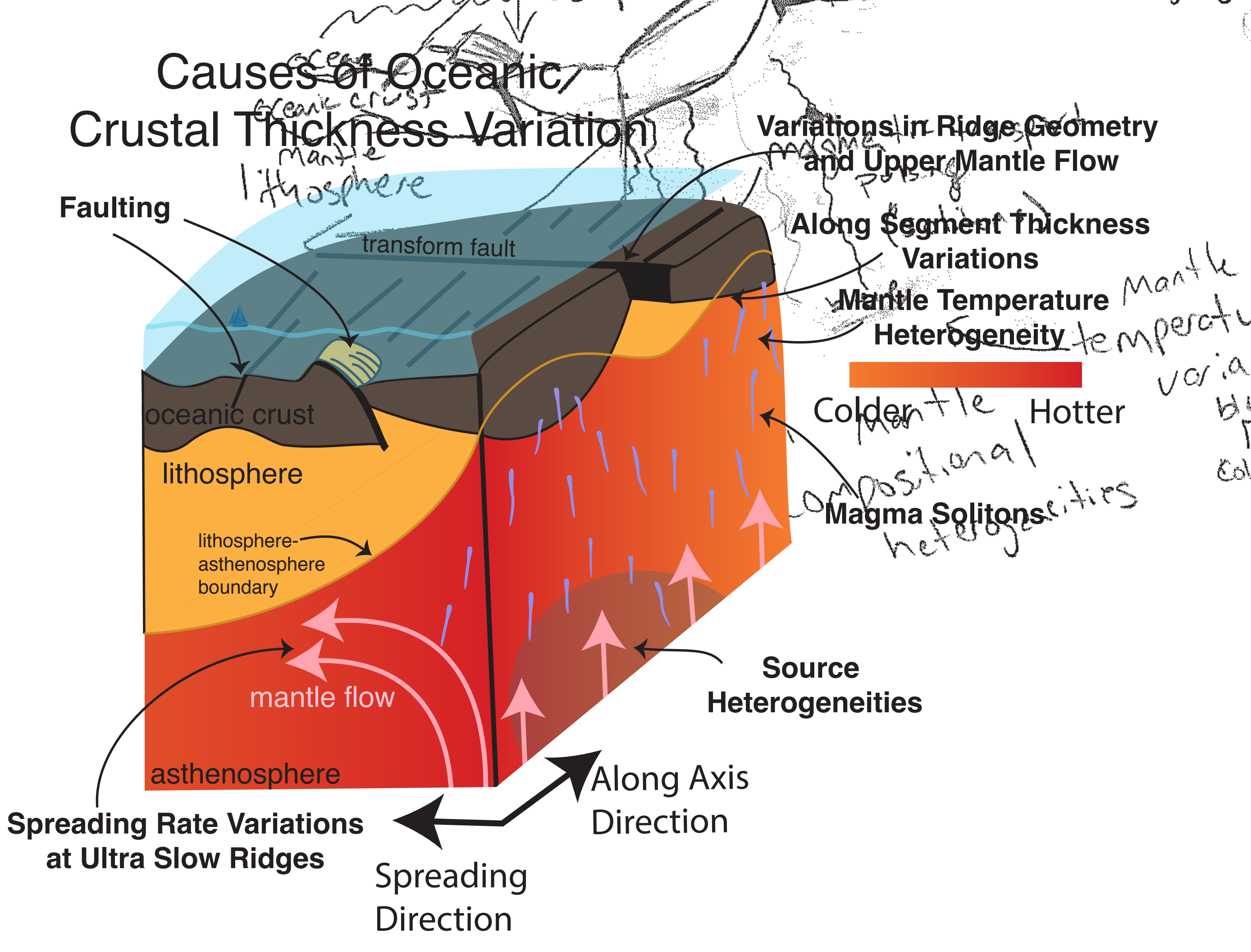

Causes of Oceanic Crustal Thickness Variation
Faulting
transform fault
oceanic crust
lithosphere
lithosphere-asthenosphere boundary
mantle flow
asthenosphere
Variations in Ridge Geometry and Upper Mantle Flow
Along Segment Thickness Variations
Mantle Temperature Heterogeneity
Colder
Hotter
Magma Solitons
Source Heterogeneities
Spreading Rate Variations at Ultra Slow Ridges
Along Axis Direction
Spreading Direction
oceanic crust
mantle
lithosphere
magma
mantle temperature
mantle compositional heterogeneities

Figure 9.

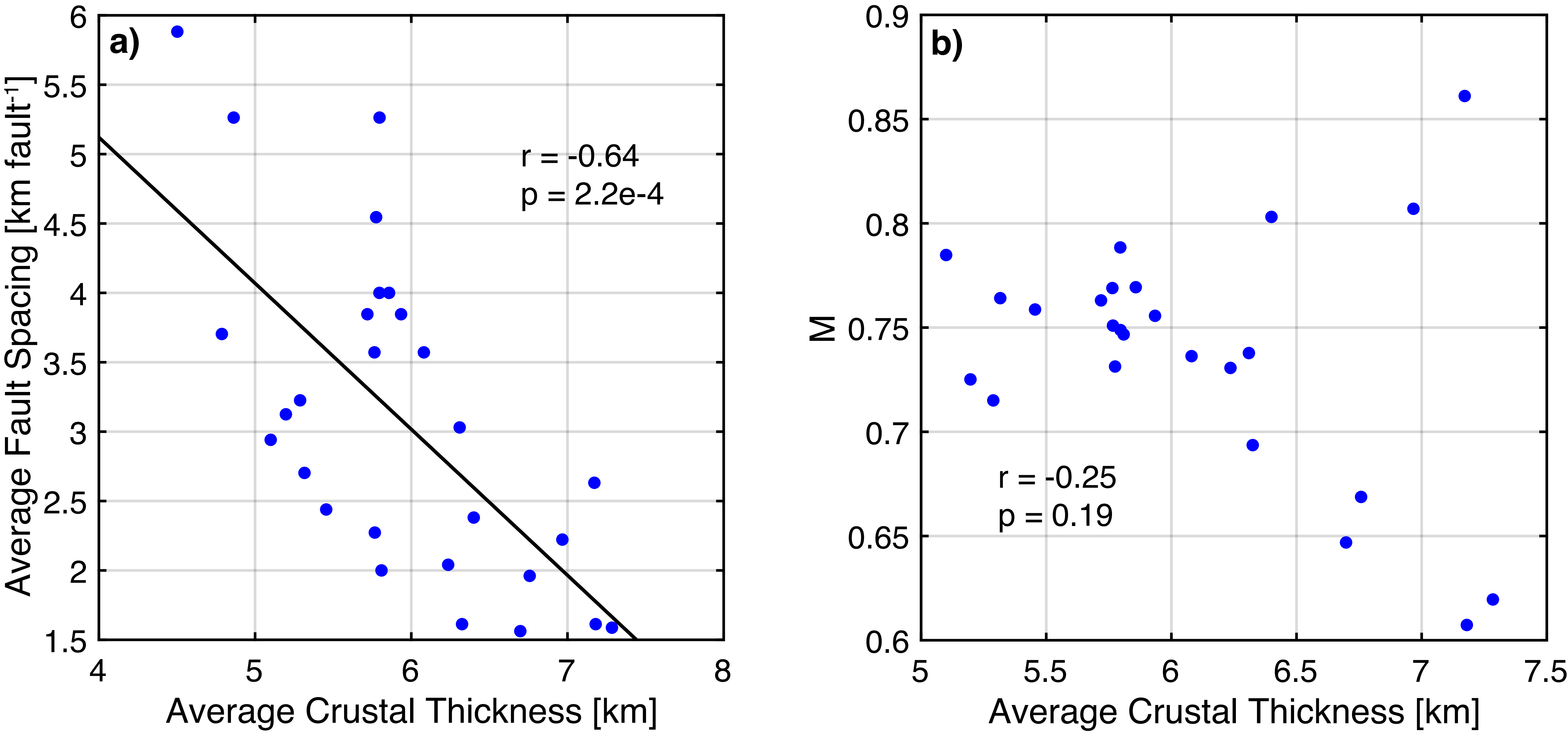

a)
r = -0.64
p = 2.2e-4
Average Fault Spacing [km fault^{-1}]
Average Crustal Thickness [km]
6
5.5
5
4.5
4
3.5
3
2.5
2
1.5
4
5
6
7
8
b)
r = -0.25
p = 0.19
M
Average Crustal Thickness [km]
0.9
0.85
0.8
0.75
0.7
0.65
0.6
5
5.5
6
6.5
7
7.5